Spatial Variations in Ancient Meteoric Water: An Investigation of the Rattlesnake Tuff

by

Julian Michael Cohen

A thesis submitted in partial fulfillment of the
requirements for the degree of

Master of Science
in
Geology

Thesis Committee:
John Bershaw, Chair
Richard Hugo
Martin Streck

Portland State University
2023

Abstract

Volcanic glass has been used extensively as a paleoclimate proxy. Deuterium (^2H) concentrations in glass have been found to be stable over geologic timescales, making δD a reliable proxy for ancient water chemistry. However, continued work revolves around better understanding how different factors affect preserved water in ash. Here, I analyze δD in the Rattlesnake Tuff (RST), a widespread ca. 7 Ma ashflow tuff, and create an isoscape to assess variations in δD across Oregon during that time. Additionally, I examine compositional data from glass shards to explore the relationship between δD and shard composition. The RST exhibits well defined compositional bands owing to its eruption from a zoned magma chamber. I investigate whether this affects δD values and should be considered in paleoenvironmental interpretations. 16 ash samples were collected across central and eastern Oregon from various flow units within the RST. Samples were analyzed for δD using a Temperature Conversion Elemental Analyzer (TC/EA) connected to a mass spectrometer and elemental composition using a Scanning Electron Microscope (SEM). I compare my isotopic results to modern water and published ancient water proxy data to better constrain changes in climate and topography across Oregon throughout the Neogene. I also estimate wt. % H_2O by calculating excess (non-stoichiometric) oxygen from SEM elemental data. My results show significant spatial variation in δD values of RST, ranging from –107‰ to –154‰. δD values of ancient glass are similar to modern water near the Cascade Mountains, but become relatively negative to the east near the inferred eruptive center of the RST. I do not observe significant variation in δD among flow units from single locations, nor do I

observe a significant relationship between wt. % H_2O and major and minor elementabundances in unprepared samples. Lastly, there is not a significant relationship between prepared glass shard composition and wt. % H_2O or δD, supporting the use of volcanic glass as a reliable paleoenvironmental indicator.

Acknowledgements

There are many people and places to thank for helping to get me through these two years. Thanks to my advisor, John, whose calm and steady demeanor helped me stay on track throughout this project. Quite a few times his gentle suggestions and ideas saved me from a lengthy spiral. Thanks also to Rick Hugo and Martin Streck, who helped me reason through difficult questions as members of my committee. Thanks to my parents, Ben and Carla, my sister, Sophie (Crabe), my grandparents, Ann and Larry, Mark and Lillian, and my girlfriend, Maggie (Margine), who have all provided me with endless love and support despite 3000 miles of separation and a pesky time difference. Next, my roommates Billy, Sam, and Madison, who helped me have a comfortable and happy home in Portland, which meant more to me than I ever realized it could. My PSU friends (cohort, as they say) Rud, Darlene, Alyssa, Obinna, Yasin, Andrew, who all shared the highs and lows of grad school with me. Thanks to each of you for the time we shared in the cave and elsewhere laughing, thinking, and commiserating. Thank you, Sherri, for your willingness to help a stranger in the desert for 2 weeks. Your enthusiasm and interest made this project possible. Thanks also to Mt. Hood, whose snowy forests gave me the freedom to unwind on many winter weekends, and to Oregon, whose dark, misty, wet surrounds soothed me.

Table of Contents

List of Tables

List of Figures

List of Abbreviations

BSD – Backscattered Electron Detector

EDX – Energy Dispersive X-Ray Analysis

HCl – Hydrochloric Acid

HF – Hydrofluoric Acid

LMT – Lithium Metatungstate

RST – Rattlesnake Tuff

SEM – Scanning Electron Microscope

TC/EA – Temperature Conversion Elemental Analysis Isotope Ratio Mass Spectrometry

VSMOW – Vienna Standard Mean Ocean Water

δD – Difference between measured deuterium and VSMOW

1.0 Introduction

The stable isotopic composition of environmental water is highly reliant on features such as topography, climate, and geographic location. Therefore, reconstructing ancient water isotopes from the rock record is one way to constrain how a landscape has changed over time. Hydrogen isotopes preserved in vitreous volcanic glass have been established as a useful proxy for understanding paleoprecipitation and paleoenvironments (Friedman et al., 1993; Cassel et al., 2009; Saylor and Horton, 2014; Bershaw et al., 2019; Sundell et al., 2019). The utility of volcanic glass as a paleoenvironmental proxy is two-fold. First, volcanic glass is known to quickly (within 10 ka of deposition) incorporate environmental water and preserve its H isotope composition over geologically significant timescales (Ross and Smith, 1955; Friedman et al., 1993; Bershaw et al., 2019). Second, volcanic glass is easily dated radiometrically, giving interpretations a reliable temporal context.

Since the beginning of the Cenozoic, the Pacific Northwest has evolved topographically, undoubtedly responsible for changes in regional climate (Wells and Snavely, 1991; Retallack, 2007; McLean and Bershaw, 2021). Previous work has aimed to better understand these changes using δD from volcanic glass and other paleoenvironmental proxies, though there is still not a consensus about their timing and spatial extent (Priest, 1990; Kohn et al., 2002; Bershaw et al., 2019; Kukla et al., 2021; McLean and Bershaw, 2021). This project constrains how stable hydrogen isotopic compositions derived from the Rattlesnake Tuff vary over space in order to better understand controls on this paleoclimate proxy as well as constrain the paleoclimate of central Oregon during the Miocene. To do this, I sampled the Rattlesnake Tuff, a

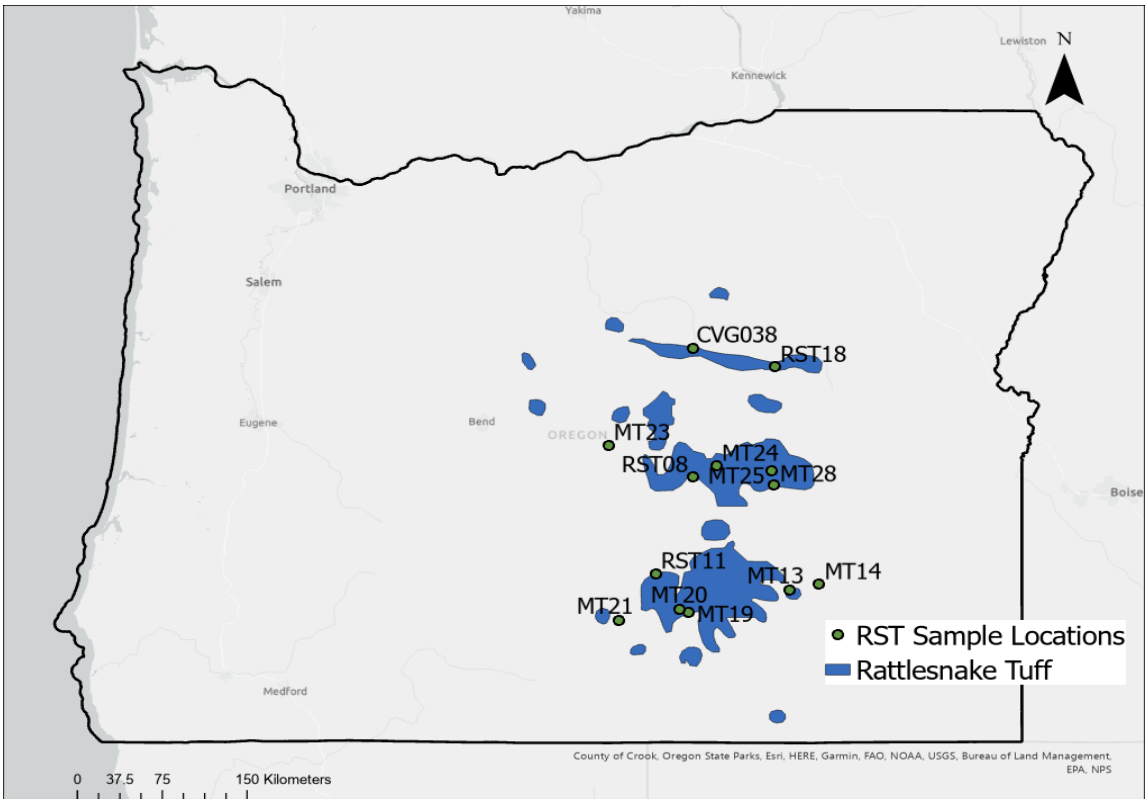

Figure 1: Map showing the spatial extent of the Rattlesnake Tuff in blue. Samples analyzed for this thesis are shown with green dots. Adapted from Streck and Grunder, 1997. Samples CVG038, RST08, RST11, and RST18 were collected by Tessa Carlson and John Bershaw in 2018.

spatially extensive Miocene ash flow tuff (Figure 1), and collected two datasets: 1) δD values for 17 samples (16 from this study, 1 from Carlson, 2018) producing a "paleoisoscape" (e.g., Caves et al., 2015) which is compared to spatial patterns in modern water δD, and 2) SEM major and minor element data to better understand compositional and textural controls on variations in δD among tuff samples. With this information, I answer the following questions: How do δD values from the Rattlesnake Tuff compare to δD values derived from modern water? How and why do isotopes in the widespread Rattlesnake Tuff ash deposit vary spatially across the Pacific Northwest? How can differences between modern and ancient isotope records be explained through changes in

climate and topography? Are any of the observed variations in δD related to changes in glass composition?

2.0 Background

2.1 Global Climate History

Through analyses of $\delta^{18}O$ in planktonic and benthic foraminifers, we know sea surface temperatures (SST) have fluctuated throughout the Cenozoic. SST fluctuations are interpreted to be indicators of changes in global climate. Between the late Eocene and early Oligocene, high-latitude SST dropped by up to 11°C (Zachos et al., 1994). These variations have continued since the beginning of the Oligocene, with well-documented periods of glaciation since ~33 Ma resulting in significant increases in oceanic $\delta^{18}O$ throughout the Oligocene and Miocene. The RST was deposited amid a global cooling episode which has been ongoing since ~15 Ma, with modern oceanic $\delta^{18}O$ and δD approximately 2 ‰ and 16 ‰ higher than they were ca. 7 Ma (Zachos et al., 2001). These differences are the result of increases in sea ice volume, which increases oceanic $\delta^{18}O$. These changes in global δD must be considered when comparing RST δD (7 Ma) to modern water.

2.2 Regional Climate History

The topographic barrier created by the Cascade Range is responsible for significant climatic variation across Oregon. West of the range, precipitation is abundant, especially in winter, and temperatures are moderate. Eastern Oregon is characterized by hot summers and cold winters, as well as very little precipitation, contributing to its classification as a desert (Figure 2). Wind-blown ash deposits of original andesitic or dacitic composition likely sourced from Cascade volcanism in western Oregon are found in the John Day region. This suggests westerly wind currents have been dominant in the

region since at least the Eocene (Robinson et al., 1990). Thus, it can be inferred that prior to the creation of a significant orographic barrier resulting from Cascade Mountain and Coast Range uplift, climate in Oregon was likely wetter in central and eastern Oregon.

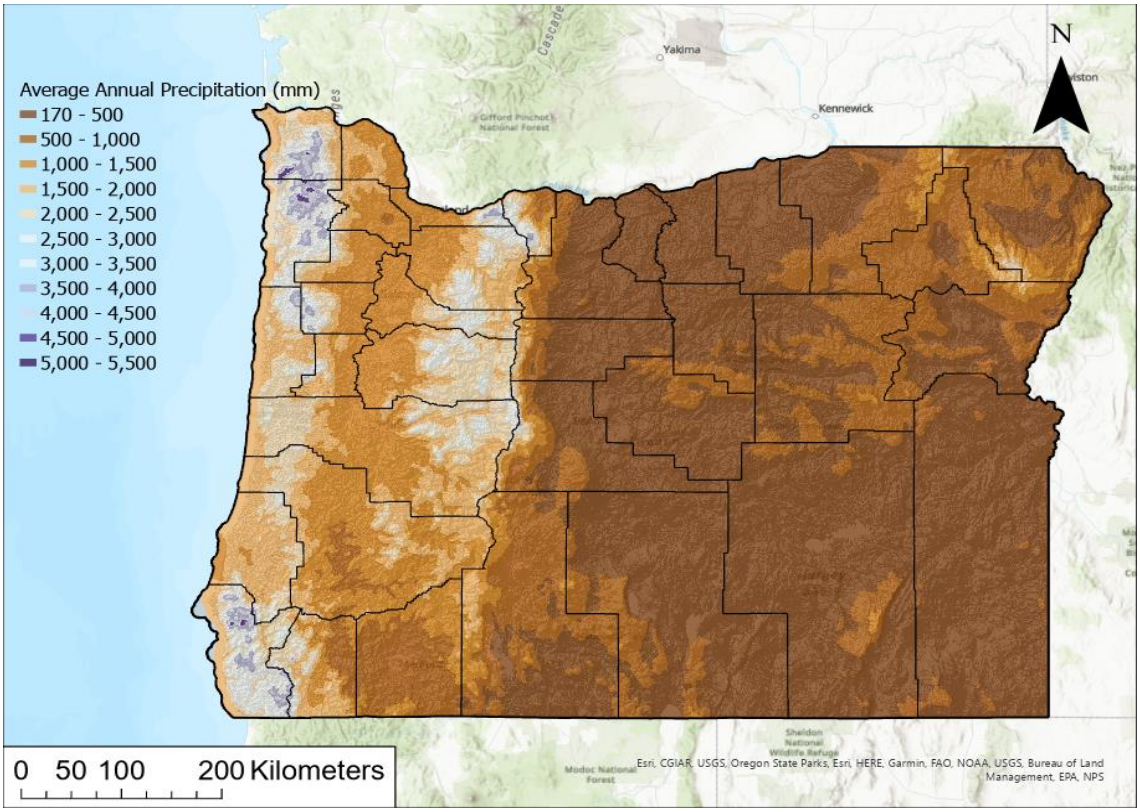

Figure 2: Modern Annual precipitation amounts across Oregon. The Cascade Range forms a significant topographic barrier, and is responsible for the arid conditions in its rainshadow, extending from central to eastern Oregon. (OSU Prism Climate Group 2022).

Researchers have used various paleoenvironmental proxies to characterize central Oregon's climate throughout the Cenozoic. Successive paleosols in the John Day region of central Oregon represent a well preserved record of these changes (Bestland, 1997). Four periods of relative warm, wet conditions in central Oregon have been interpreted at approximately 35 Ma, 16 Ma, 7 Ma, and 4 Ma (Retallack, 2007), based on chemical

weathering and the presence of carbonate nodules in paleosols and temporal alignment with times of global climate change. Retallack (2007) argues that terrestrial paleosol data are preferred over the marine oxygen isotope record because the latter is also influenced by changes in global ice volume and ocean salinity, among others (Retallack, 2007). The similarity between paleosol and marine carbon isotope records suggests Cenozoic climate in Oregon was significantly influenced by changes in atmospheric SST (Retallack, 2007). Zachos et al. (2001) provide numerical data on $\delta^{18}O$ fluctuations throughout the Cenozoic, and a means of comparing ancient isotope values to modern.

2.3 Miocene Volcanism in Oregon

The Cascade Range, a continental volcanic arc, developed into the range we see today over the Cenozoic (Wells and Snavely, 1991), but details related to the timing of rock uplift and changes in surface elevation are not well understood. There are two leading hypotheses regarding the topographic evolution of the Cascades. The first suggests that significant orographic uplift didn't occur until the mid-late Miocene and has continued until today (Kohn et al., 2002; Takeuchi and Larson, 2005; Kohn and Law, 2006). Others suggest that the Cascades have been a significant topographic barrier since the beginning of the Miocene or even before (Retallack, 2004; Bershaw et al., 2019; McLean and Bershaw, 2021). Significant voluminous Cascade Arc volcanism began around the beginning of the Oligocene (~35 Ma) (Wells and Snavely, 1991).

During the mid-late Miocene, many significant volcanic centers were active in eastern Oregon, likely genetically related to the ca. 16-17 Ma Columbia River Basalt Group (CRBG) (Cahoon et al., 2020) based on similar ages. The High Lava plains is a

highly active region of bimodal eruptive centers responsible for generating significant, voluminous, volcanic ash flow tuffs and basalts (Greene, 1973; Streck, 1994; Streck and Grunder, 1995, 1997; Streck and Grunder, 2012; Streck et al., 2015b, 2015a; Swenton and Streck, 2022; Swenton et al., 2022). It is likely genetically related to the CRBG. The Rattlesnake Tuff was erupted from the western Harney Basin and is one of two ignimbrites in the region (Streck and Grunder, 2012). Overall, the High Lava Plains were a westward-younging bimodal volcanic province that lies on the northern end of the Basin and Range extensional province (Jordan et al., 2004).

2.4 Rattlesnake Tuff

The Rattlesnake Tuff is a widespread late-Miocene ash-flow tuff that erupted from the Harney Basin ~7 Ma (Streck, 1994; Streck and Grunder, 1995, 1997). Approximately 46% (130 km^3) of the reconstructed original erupted volume (~280 km^3) remains (Streck, 1994), and just 26% (9250 km^2) of its original spatial extent remains (Streck and Grunder, 1995; Swenton and Streck, 2022). Most commonly, it is found as a 10-20m thick rimrock at plateau tops (Streck, 1994; Streck and Grunder, 1995). It is up to 60m thick and often crops out as a single unit (Streck and Grunder, 1997). The RST was likely erupted rapidly, evidenced by its cooling as a single unit (Streck, 1994; Streck, 2004). The RST characteristically displays banded pumice as well as dark brown to clear, vitreous glass shards (Streck, 1994; Streck and Grunder, 1997). It is interpreted that progressive eruption of increasingly primitive magmas resulted in glass shards with varying iron content. In places, the RST overlies a cobble conglomerate, as described by Streck and Ferns (2004). The RST is crystal poor (< 1%) and > 75 wt. % SiO_2 (Streck

and Grunder, 1997). Carlson (2018) reported significant surface precipitates on shards and in pores of less welded tuffs.

2.5 Hydration of Volcanic Glass

Previous work has shown that felsic volcanic materials are typically deposited with a small amount (~0.1 - 0.5 wt %) of primary magmatic water (Giachetti et al., 2015; Seligman et al., 2016). The amount of water remaining in a glass is largely a function of the nature of the eruption (Seligman et al., 2018). Slow, effusive silicic eruptions can degas nearly completely (~0.1 wt% H_2O), while more rapid, explosive eruptions retain more of their original magmatic water (up to ~0.6 wt%) (Seligman et al., 2018). While magmas typically have higher water concentrations than this (2-6 wt. %), degassing during eruption causes most magmatic water to degass (Seligman et al., 2016). While the amount of magmatic water remaining in glass is relatively small, it does have potential to influence the isotopic composition of volcanic glass that is minimally hydrated by meteoric water. Under this scenario, magmatic water could theoretically account for up to ~20% of water in glass at the time of analysis. This number is based on Seligman's (2018) estimate that volcanic glass from explosive eruptions can retain up to 0.6 wt. % H_2O, and an average wt. % H_2O in my samples of ~ 3.0 (Seligman et al., 2018). If a sample containing 3.0 wt. % H_2O with a δD of -130‰ were contaminated with 20% magmatic water, one would expect a maximum shift in δD of approximately +14‰. This estimate assumes the δD of magmatic water to be -60‰, an upper extreme derived from glass erupted from Mt. Saint Helens (Seligman et al., 2018). Additionally, one would expect to see an inverse relationship between wt. % H_2O and δD if a significant amount

of magmatic water remains in some samples. That said, the isotopic composition of volcanic glass is more likely to reflect ancient environmental conditions if they are hydrated to > 2 wt. %, as this more often leaves a negligible amount of residual magmatic water relative to meteoric water (Cassel and Breecker, 2017). Giachetti et al. (2015) determine that highly explosive eruptions likely retain even less of the original magmatic signal (0.2 – 0.5 wt. %). Newly erupted volcanic glasses are typically hydrated by meteoric water for up to 10 Kya, after which a gel layer develops that prevents further exchange with the environment (Cassel and Breecker, 2017; Jimenez-Rodriguez et al., 2023). This preserves the isotopic composition of meteoric water in the environment at the time of ash deposition (Saylor and Horton, 2014; Cassel & Breecker, 2017; Carlson, 2018; Sundell et al., 2019; Jimenez-Rodriguez et al., 2023). However, Cassel and Breecker (2017) suggest that some secondary processes can cause destruction of the passivating layer and resumption of meteoric water diffusion.

2.6 Modern δD Influences in Oregon

Environmental factors that influence the isotopic composition (δ^2H or δD) of modern meteoric water are well known. Increasing elevation and latitude (lowering temperature) have been shown to cause a decreases in the isotopic composition of atmospheric vapor (Dansgaard, 1964; Rozanski et al., 1993). The concentration of deuterium in meteoric water is heavily reliant on additional environmental factors such as moisture source, relative humidity, and vegetative cover (Rozanski et al., 1993; Gonfiantini et al., 2001; Poage, 2001; Tian et al., 2007; Lee & Fung, 2008). In Eastern Oregon, variations in δD are likely the result of changes in elevation, distance from the

ocean (moisture source), or evaporative enrichment due to relatively arid conditions in the rain shadow of the Cascade Mountains (Dansgaard, 1964; Rozanski et al., 1993; Bershaw et al., 2020). A gradual depletion of δD is observed eastward across Oregon (Figures 3 and 4), consistent with deuterium behavior in rain shadow systems. Most precipitation falls on the windward side Cascade mountains, effectively depleting the atmosphere of deuterium over the eastern part of the state, a phenomenon known as the "altitude effect" (Rozanski et al., 1993). Further expressions of these phenomena are observable in other parts of eastern Oregon, including the relatively high elevation Blue Mountains in the northeast which cause a marked decrease in δD values. δD continues to

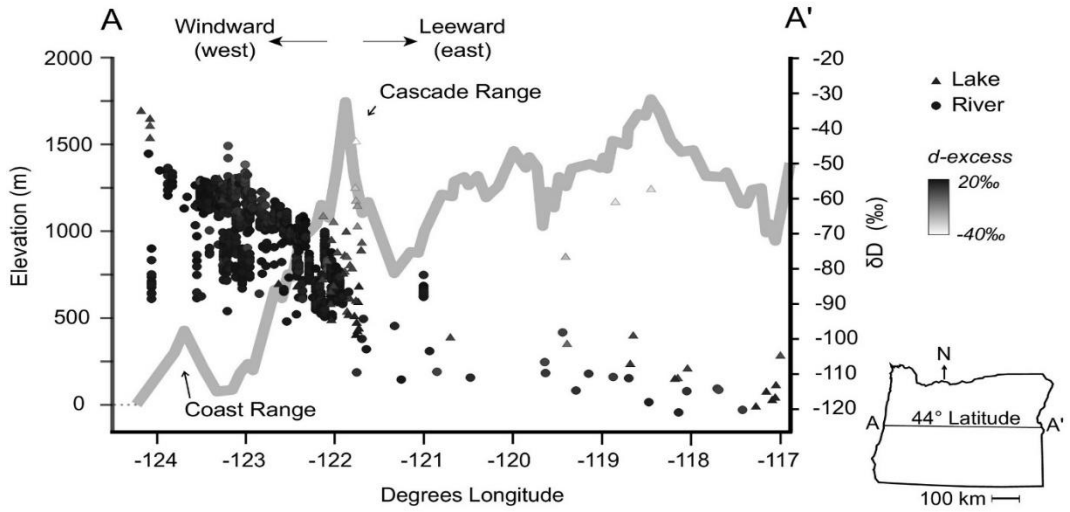

Figure 3: Elevation profile from W-E along the 44th latitude (solid line). Modern δD values are represented by various shapes. From Bershaw et al. (2019).

decrease eastward across central and eastern Oregon, but more modestly, consistent with the "continental effect" (Rozanski et al., 1993). Globally, the average isotopic lapse rate for δD is -22.4‰/km elevation gain (Poage and Chamberlain, 2001). Near the study area in the Ochoco Mountains, the isotopic lapse rate is similar at -26.4‰/km (Greenwood, pers. comm. 2023).

To better constrain the controls on modern water stable isotopic variations in central Oregon, I created three sets of linear regressions for each of the major global isotopic controls (amount, continental, altitude) (e.g. Dansgaard, 1964; Rozanski et al., 1993). Data considered in these analyses was filtered to only include samples collected in rivers and streams east of the Cascades. Additional fields for elevation and precipitation were added from respective rasters (NOAA, 2000; OSU PRISM, 2023). Regression analyses were performed only using datapoints that had δD, location, elevation, and precipitation data.

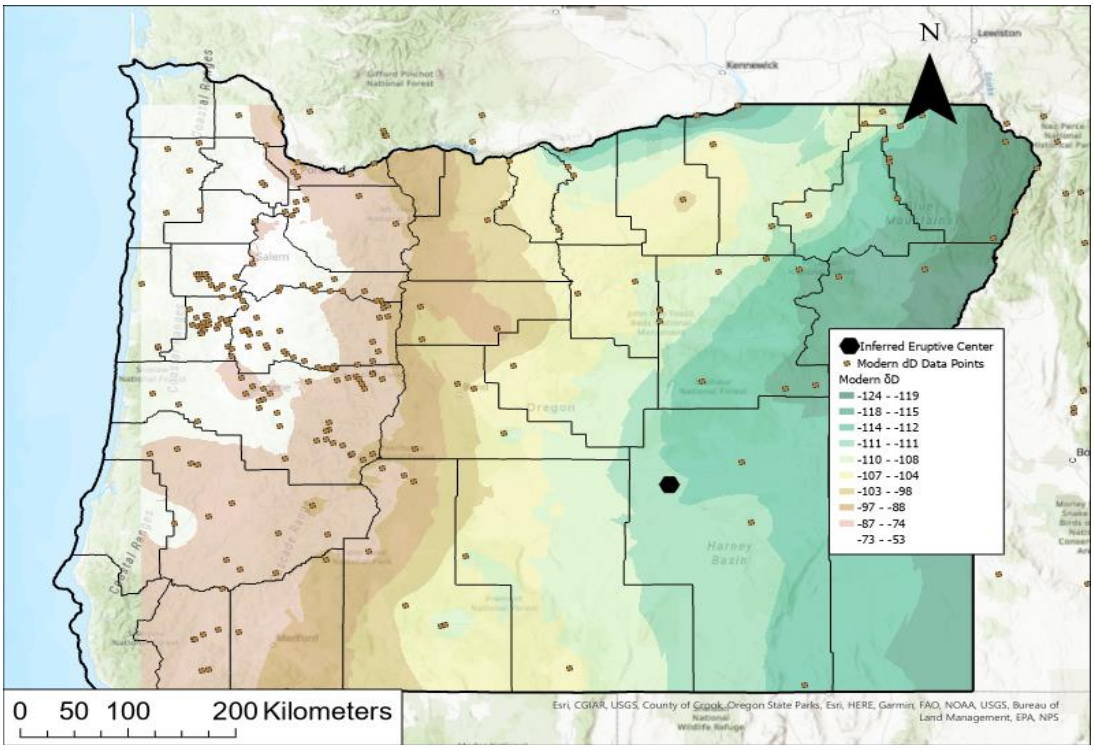

Figure 4: Map showing modern δD values based on stream and precipitation water samples collected in Oregon (Waterisotopes Database 2022). The interpolated surface was made with the Kriging interpolation tool in ArcGIS Pro. A trend towards lower δD values can be observed eastward. The inferred eruptive center refers to the RST.

2.6.1 Amount, Continental, and Altitude Effects

Lee and Fung (2006) summarize and model three processes associated with the amount effect that result in fluctuations in δD in both the atmosphere and in actively falling precipitation. Generally, the amount effect describes fractional removal of heavy isotopes (deuterium) in the atmosphere related to condensation and precipitation (Dansgaard, 1964; Rozanski et al., 1993; Lee and Fung, 2006). However, additional fractionation occurs during evaporation as rain drops fall to the ground surface. Here, ambient temperature, drop size, and fall velocity dictate the degree to which lighter isotopes are lost. Regions with heavy rainfall, higher humidity, and milder temperatures experience less post-condensation fractionation than relatively arid regions with less deep convective precipitation (thunder storms).

In Oregon, annual precipitation amounts vary significantly across the state (Figure 2). This is due largely to the presence of the Cascade Mountains, which produce a rain shadow effect resulting in a dry leeward side of the range, and isolated topographic highs such as the Blue Mountains and Steen's Mountain, which receive higher annual precipitation amounts than the areas that surround them (Figure 2). Overall, the annual precipitation amount and modern δD values do not show a significant relationship (R^2=0.02), indicating that the amount effect does not play a consequential role in shaping modern water isotopes across central and eastern Oregon. However, there is topographic variation throughout central and eastern Oregon that does appear to affect the isotopic composition of water. Figure 5 shows that generally, areas with lower δD values are clustered around areas of higher elevation. The effect of elevation on δD in central and eastern Oregon is shown to be moderate (R^2=0.34). Also, we do see a relatively strong

relationship between longitude and δD (R^2=0.83) across central and eastern Oregon, suggesting that the continental effect has the greatest effect on δD out of the three considered.

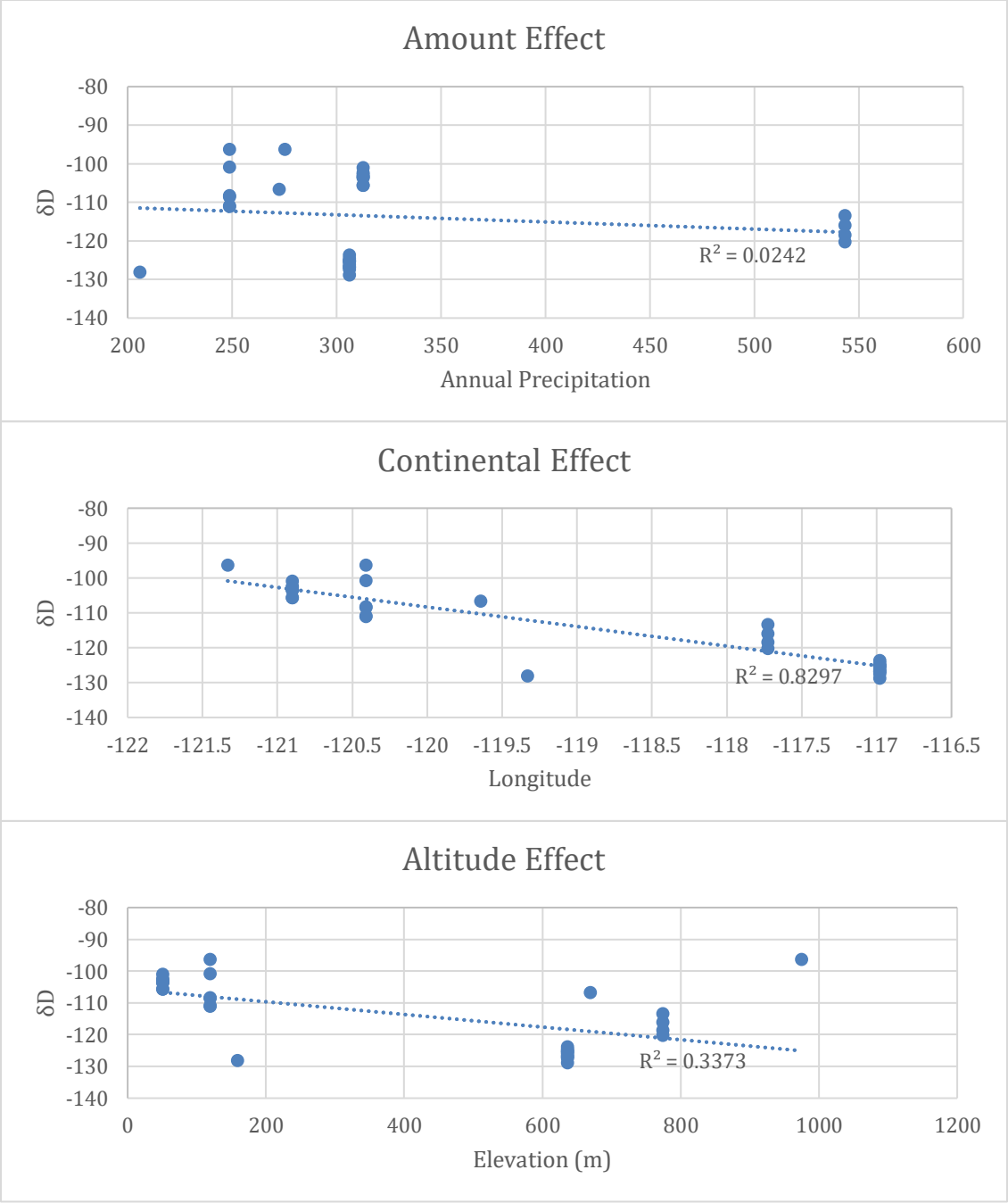

Figure 5: Graphs showing the effects on δD over space in central Oregon. R^2 values show relative influence of each effect, but are not reflective of overall influence. In general, modern central Oregon is dominated by the continental effect, with the amount effect playing very little role in spatial δD variation. Modern δD data in this figure are from waterisotopesdatabase.org, elevation data are from DOGAMI, precipitation data are from OSU Prism Climate Group.

2.7 SEM Procedures

2.7.1 Backscattered Electron Analysis

The backscattered electron detector (BSD) provides qualitative compositional data in the form of grayscale colorations. In this scheme, brighter (higher) grayscale values correspond to elements with higher atomic numbers, while darker (lower) grayscale values correspond to elements with lower atomic numbers. Analysis of grayscale distributions using ImageJ, an image processing software, can reveal qualitative information about distributions of relatively light and heavy elements.

2.7.2 Energy Dispersive X-ray Analysis

Energy-dispersive X-ray (EDX) analysis provides quantitative compositional data based on the energies of X-rays emitted by a sample following excitement by an electron beam. For each element, a wt. % is calculated independent of other elements by evaluating the relative amount of each detected X-ray. Results of this analysis can be expressed as normalized or unnormalized totals. Normalized totals always add up to 100%, while unnormalized totals typically do not as a result of each element's wt. % being calculated independently. Analytical uncertainties associated with these analyses are typically +/- 0.5 wt. %, or 3σ.

2.7.2.1 Excess Oxygen

Hydrogen is undetectable by the EDX detector. Thus, it is not possible to directly measure how much water is in a sample. Instead, we make a series of assumptions to estimate the amount of water in a sample stoichiometrically. This involves using wt. % O calculated in two different ways. First, O can be directly measured by the EDX detector.

Second, in geologic samples, it is also common to estimate the amount of oxygen by assigning stoichiometrically based on the presence of common O-bearing molecules. The difference between these numbers, when O measured by the EDX detector is greater than O calculated stoichiometrically, is assumed to represent the wt. % O in the sample as a part of water molecules, which are bonded to undetectable hydrogen atoms.

3.0 Methods

3.1 Sample Collection

Samples were collected from various outcrops located in central and eastern Oregon during an approximately 2-week field campaign during August 2022 (Figure 1). Target samples were non to partially welded, with abundant glass and low degrees of weathering. In this thesis, weathering is understood to mean the presence of secondary mineralization and oxidation on the surface of glassy shards. All samples considered in this document contain glassy shards. For the Rattlesnake Tuff, this means samples were typically collected from the non-welded basal portion of the tuff. Spatial diversity was an important consideration in selecting sample locations. Approximately 1 kg of sample was collected from 10-30 cm into the outcrop surface to reduce the influence of weathering and oxidation. This improved the chance that samples contained pristine glass, and that there was enough material to be properly processed.

3.2 TC/EA Sample Preparation

Currently, there are two accepted methods for preparing volcanic glass samples for isotopic analysis (Carlson, 2018). The methods I employed are outlined by Cassel and Breecker (2017) and use hydrofluoric acid (HF) treatment to effectively remove surface contaminants (Carlson, 2018). Samples were crushed with a ceramic mortar and pestle. After crushing, a small amount of sample was placed on a glass slide in immersion oil. Based on petrographic analysis, samples with plentiful vitric glass were selected for further preparation.

3.2.1 Sieving

Selected crushed samples were wet-sieved using nylon screens with 150 and 70 μm filters. Up to four 1L beakers were needed to fully wash each sample. All size fractions were archived in plastic bags with appropriate labels. Sieved samples were dried in an oven overnight at 60℃.

3.2.2 Acid Abrasion

The filtered 70-150 μm fraction of glass shards were washed two to three times in 10% hydrochloric acid (HCl) for 30 seconds to remove carbonates. Samples were then washed one to two times in 8% HF for 30 seconds. This removed contaminants still bonded to the surface as well as the outermost layer of potentially altered glass. Cassel and Breecker (2017) conduct two 30-second HF washes, suggesting variability in δD measurements is reduced after the second wash. However, HF also quickly dissolves glass, meaning that some samples may be destroyed by prolonged exposure. Therefore, not all samples were washed with HF twice.

Following acid washing, some samples were completely devoid of pristine glass shards so were unusable. After drying overnight in the oven at around 60℃, all samples formed a layer of precipitates on top. The precipitate layer in glassy samples normally breaks apart with a couple taps of the beaker (or glass shard container) on the counter. Samples without usable glass (likely mostly clay) did not break apart easily when tapped on the counter, and even with a tool such as a small metal spoon were difficult to separate. These samples containing clays were not suitable for paleoenvironmental analysis so were discarded.

3.2.3 Removal of Magnetic Shards

Magnetic minerals were removed with a hand magnet. Samples were poured onto a clean, flat surface (such as a folded piece of printer paper). The magnet was passed over the sample, using the flat edge of the magnet to distribute the sample into a thin, even sheet. This ensured that all magnetic grains were able to contact and stick to the magnet. Because grains are small (70 - 150μm), some nonmagnetic grains also stuck to the magnet. To ensure these nonmagnetic grains were not removed from the sample, the magnet was tapped gently on its side prior to scraping the magnetic shards off of the magnet. In some cases, well over half of the sample grains were removed by the magnet. I assessed whether metallic samples caused variation in my results by analyzing both magnetic and nonmagnetic shards from the same outcrop and found that there was no significant difference in δD measured in magnetic and nonmagnetic shards. This suggests that there may be no reason to remove magnetic grains if a sample is purely composed of glass.

3.2.4 LMT heavy liquid separation

Samples were further sorted through gravity separation using heavy liquid lithium metatungstate (LMT). Removing magnetic shards before heavy liquid separation allowed for more effective density separations. The LMT was diluted to 2.7 g/cm^3 to match the desired density of "pure" glass shards. This systematic approach to sample preparation was vital to ensure that only pristine glass shards were selected for analysis. However, it also required the collection of a large mass of sample (at least 1 kg), as in some cases, sample preparation left only 10-20 mg of the original material.

3.3 Microscopy and Microanalysis Sample Preparation

3.3.1 Analysis of Alteration of the Passivating Layer by Ambient Conditions

Sample MT-23 (Figure 1) was collected from float directly beneath an outcrop approximately 10 miles southwest of Paulina, OR along Van Lake Road. It was chosen for analysis because it contains abundant glass and has a distinct oxidation rind, making it easy to compare oxidized and unoxidized portions. I sought to establish whether the formation and oxidation of secondary minerals on shard surfaces was affecting water content. Some interactions between ambient substances and the shard surface can result in alteration of the passivating layer and the resumption of diffusion of meteoric water into the shard (Cassel and Breecker, 2017). For SEM analysis, samples were lapped and polished to a perfectly flat surface. This ensures signal is not lost as it exits the sample, as rough surfaces absorb electrons exiting the sample. A small block (1 x 3 cm, Figure 6) was cut and impregnated with epoxy. After at least 24 hours of curing, the sample was polished for analysis in the SEM (Figure 6). For optical analysis, samples were crushed using a mortar and pestle and then filtered to only include shards between 70-150μm. Shards were then placed in immersion oil to create temporary glass slides. This was done for shards with and without secondary surface minerals.

3.3.2 Glass Shard Compositional Analysis

Following TC/EA analysis, 14 of the 16 samples prepared for TC/EA analysis were prepared for compositional analysis using the SEM EDX detector. The two samples not prepared (MT-28a and MT-28bm) were skipped because they were donated to the Light Stable Isotope Laboratory at the University of Texas, Austin to be used as standards.

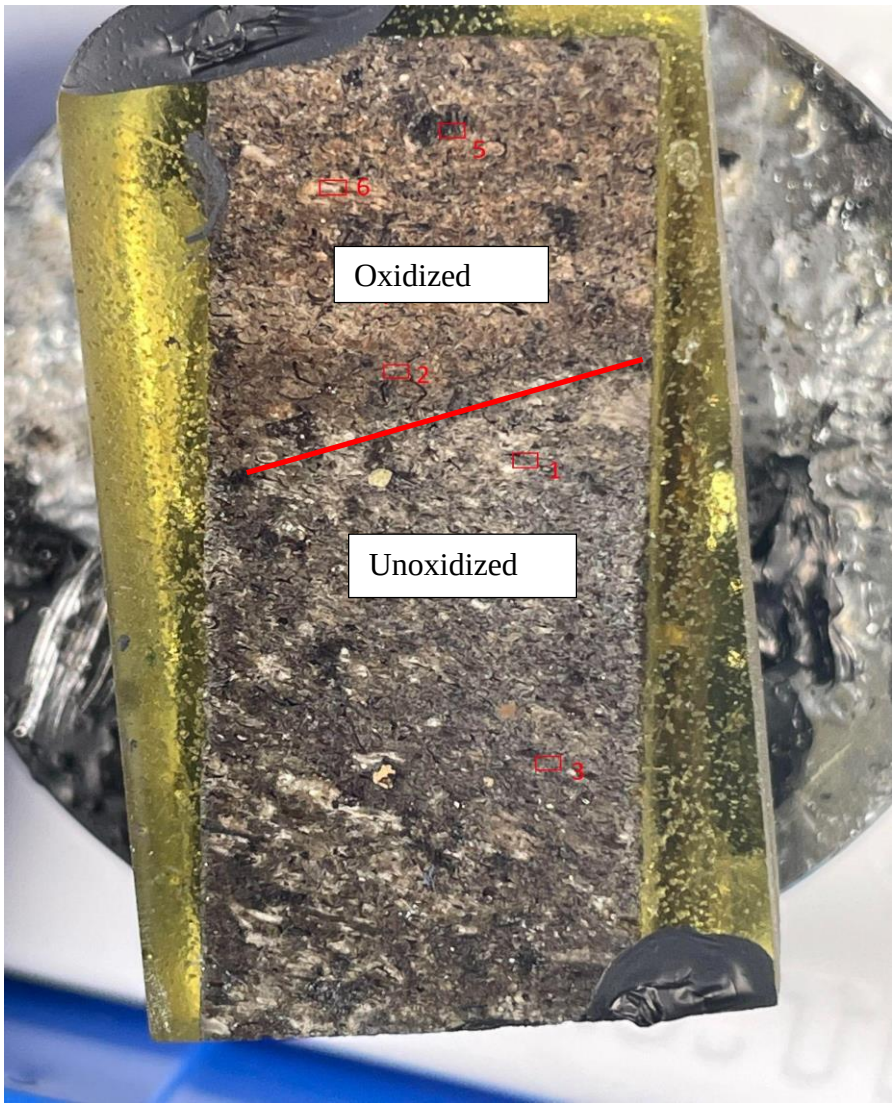

Figure 6: Block cut from sample MT-23, analyzed for properties of oxidized (top) vs. unoxidized (bottom) sections in the SEM.

Approximately 5-10 mg of each sample was poured into a plastic mounting cup. A piece of double-sided tape was cut to fit in the bottom of the cup and adhered to the bottom, with the up-facing adhesive side serving to hold the glass shards to the bottom of the cup. Next, epoxy was mixed and poured into each cup, which were left under a vacuum at room temperature to remove excess bubbles from the epoxy. Finally, samples were left to fully cure under a fume hood.

3.4 TC/EA Sample Analysis

A total of 16 samples were analyzed using the TC/EA High Temperature Conversion Elemental Analyzer (TC/EA) Isotope Ratio Mass Spectrometer at the University of Texas at Austin's Light Stable Isotope Laboratory. Each sample and standard were weighed into three ~6 mg silver foil capsules for analysis. All samples and standards were run in triplicate to ensure measurements were unaffected by previous analyses. The TC/EA allows for up to 49 individual silver foil capsules (16 triplicated samples) to be run at once. Thus, including all samples and standards, two ~7-hour analytical sessions were required.

3.5 TC/EA Data Analysis

Data were reported as δD_{glass} and converted to δD_{water} using the following equation from Friedman et al. (1993).

$$\delta D_{water} = \left(\frac{1000+\delta Dglass}{0.967}\right)\text{-}1000 \quad [1]$$

This conversion allows for a direct comparison between ancient δD values derived from glass analyses and δD values obtained from modern water samples. Converted values

were used to create paleo-"isoscapes" (Figure 5), which were generated using the kriging interpolation tool in ArcGIS Pro. This calculated a δD value for every cell in a raster whose dimensions are limited by the spatial distribution of the samples. The same steps were applied to modern water data, which was sourced from waterisotopesdatabase.org.

3.6 SEM Sample Analysis

Because the Rattlesnake Tuff exhibits a variety of different lithologies (characteristic banded tuff) due to its complex petrogenetic history, I analyzed compositional variations in glass samples to determine whether they affect the isotopic composition or wt. % water of glass. An assumption critical to the validity of this methodology is that measured δD in ancient glass samples is representative of environmental conditions at the time of eruption, rather than sometime after deposition, and is unaffected by other factors such as rock chemistry. Volcanic glass can undergo a variety of weathering and alteration processes such as devitrification, leaching, and secondary mineralization, all of which have the potential to overprint paleoclimate signatures. Because of this, a rigorous methodology for selecting "pristine" glass shards was used (Cassel and Breecker, 2017). An important step in this process was the initial sample selection, which involved viewing crushed samples in both plane- and cross-polarized light using a petrographic microscope. A sample was deemed acceptable if it contained ample pristine (unaltered) glass. While past studies have suggested that this procedure is effective for isolating unaltered glass (Cassel and Breecker, 2017; Carlson, 2018; Bershaw et al., 2019), scanning electron microscope imaging provides a way to verify observations from the petrographic microscope. In this study, I used the SEM to

gather both chemical and textural data of glasses that exhibit secondary mineralization on their surface and those that do not to independently determine their suitability for analysis. Following δD analysis, the SEM was employed a second time to clarify any relationship between glass composition and glass isotope ratios or wt. % water.

3.6.1 Effect of Oxidation and Surface Mineralization on Water Content in Untreated Tuff

I utilized the BSD and Energy-Dispersive X-ray Spectrometer (EDX) detectors to collect average Z and chemical data. Using the BSD detector, I imaged both oxidized and unoxidized glass shards and compared them, looking specifically for shards that have distinct internal variation in BSD grayscale brightness. Once these were found, I used the EDX detector to gather chemical data in areas with interesting BSD contrast (Figures 7 and 8).

3.6.2 Compositional Variations in Prepared Glass Shards

Five samples were selected for analysis based on their δD and wt. % H_2O. Samples RST2018-08 (low Fe content), MT-21 (high δD), MT-28b (low δD), MT-28dm (high Fe content), and MT-13c (high wt. % H_2O) were chosen to evaluate the effects of glass shard composition on δD and wt. % H_2O. Samples were run in two separate batches due to space limitations inside of the SEM. For each sample, 30 spectra were collected. Gathering spectra with acceptably high totals was a challenge, as the SEM revealed that despite careful polishing, many of the shards still had badly pitted and irregular surfaces.

3.7 SEM Data Analysis

3.7.1 Effect of Oxidation and Surface Mineralization on Water Content in Untreated Tuff

From my preliminary analyses, I obtained 69 individual measurements across 6 different sites (Figure 8) in the oxidized and unoxidized sections of the sample. Data were accepted if their unnormalized totals were between 90% and 105%. Results were exported as tables, with totals calculated both with the "All Elements" and "O by Stoichiometry" settings in AZtec. A total of 12 tables were exported; two for each site. To assess the presence of water, excess oxygen was calculated by subtracting wt. % O from stoichiometry from wt. % O directly measured with EDX. The result, if positive, reflects that some O is bonded to hydrogen, which is undetectable with EDX. We assume that this excess O is representative of water in the sample. Images were also analyzed in ImageJ, where the BSD grayscale value for each measurement was measured in 16-bit. The results of each of these two processes were plotted in x-y space (Figure 9). Additionally, the means were compared using a two-mean t-test to assess for similarities in the populations (Figure 10).

3.7.2 Glass Shard Composition

Using the programming language R, the data table was manipulated so that results could be plotted by sample and by element. Statistical outliers were removed if their unnormalized totals were below 70%. I concluded that outliers below this threshold were not reliable enough to be considered in my analysis. To correct for this, totals were normalized to 100%. Once the data were reformatted, boxplots comparing the wt. % of

each sample by element were plotted (Figure 10). Finally, ANOVA tests were run to determine if any samples contained anomalous elemental concentrations (Table 1).

4.0 Results

4.1 SEM Results

4.1.1 Effect of Oxidation and Surface Mineralization on Water Content in Untreated Tuff

Preliminary backscattered electron images revealed that oxidized glass shows more fracturing and precipitates between grains compared to pristine glass (Figure 7). Preliminary Backscattered Electron Detector (BSD) images (Figure 7) also shows brightness gradients from the center to edge of oxidized shards that are not visible in unoxidized shards. This is evidence that there may be more differences between oxidized and unoxidized shards than are visible through petrographic microscopy.

To examine this, I obtained 69 compositional datapoints from 6 sites (Figure 8, Appendix C-1). When plotted in x-y space (Figure 9), it is clear that the two populations are very similar. The oxidized tuff has a mean excess O of -3.88 and a mean grayscale of 89.22, while the unoxidized tuff has a mean excess O of -2.62 and a mean grayscale of 83.74. Despite these differences, the unoxidized tuff plots directly on top of the oxidized tuff, though does have much less variation; especially in excess O (Figure 9). This highlights that the two tuffs have very similar BSD grayscale and excess O despite oxidation and surface precipitate differences. The two-mean t-tests show that there is no significant difference in excess O between the oxidized and unoxidized datasets, but there is a significant difference between the grayscales (Figure 10).

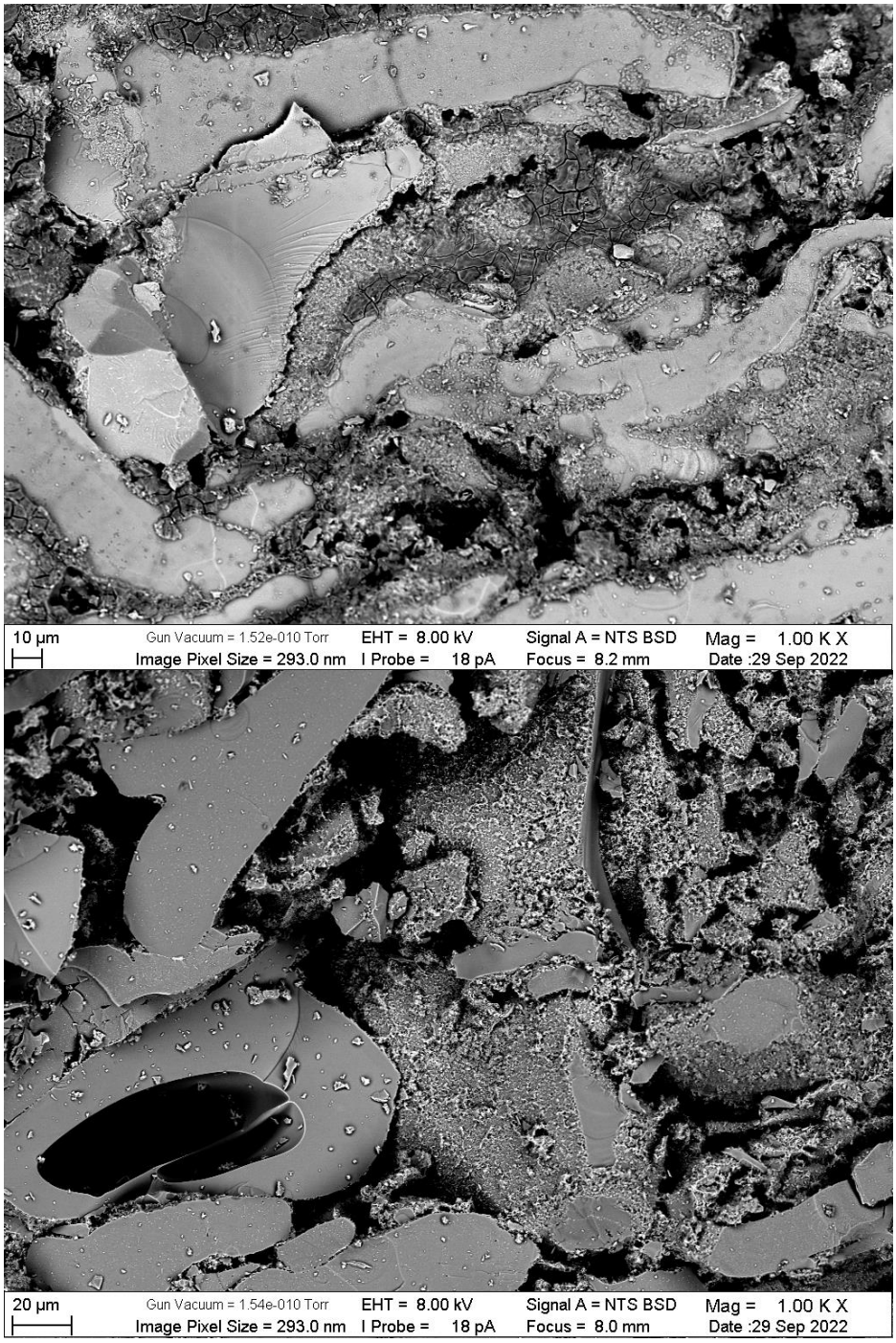

Figure 7: Backscattered Electron images of sample MT-13c. the top image was taken within the oxidation rind to show secondary mineralization textures in pore spaces and on shard surfaces. The bottom image shows fewer secondary minerals forming outside of the oxidation rind.

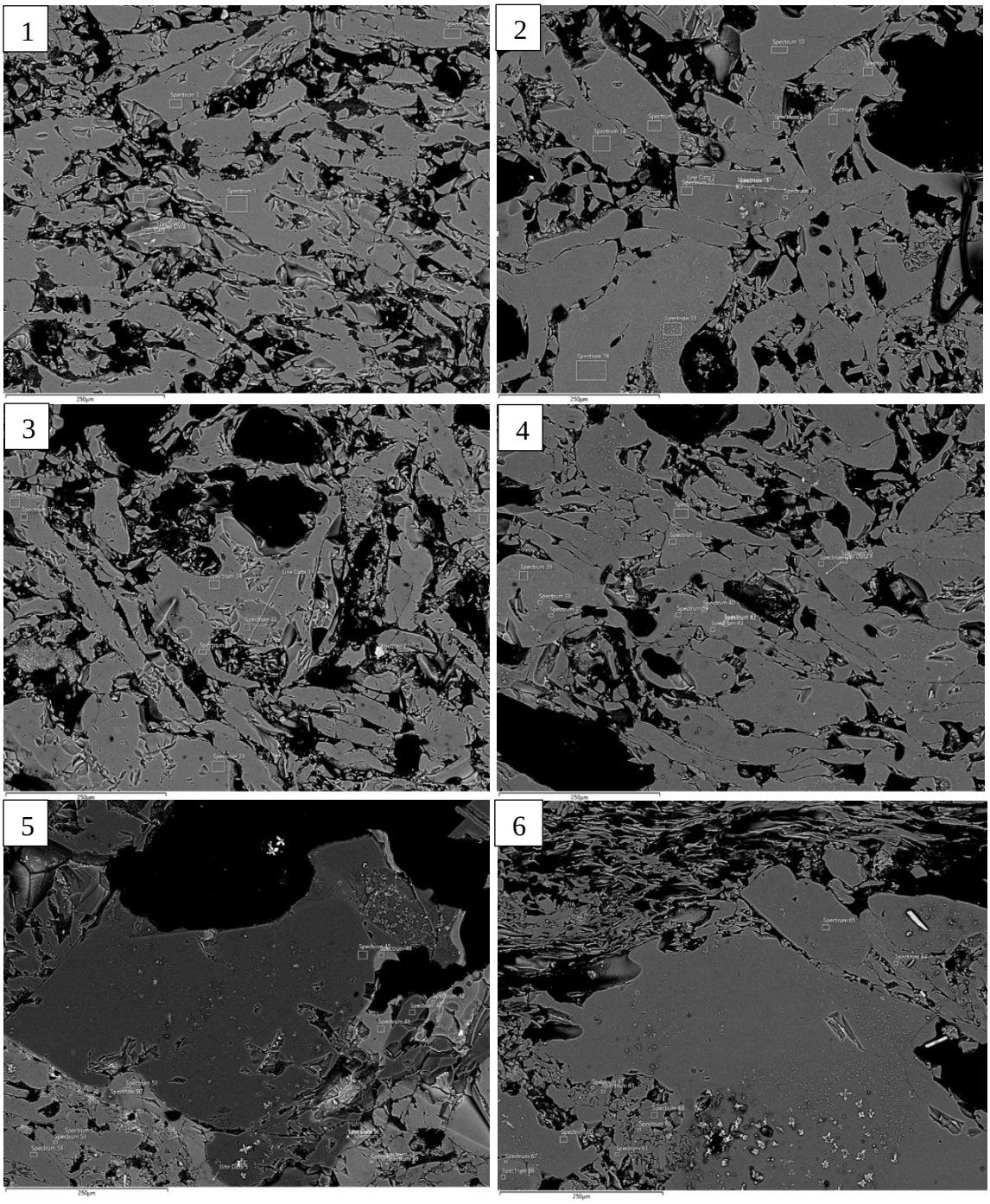

Figure 8: Backscatter images of sample MT-23. Sites 1 and 3 are in the unoxidized section, while sections 2, 4, 5, and 6 are oxidized.

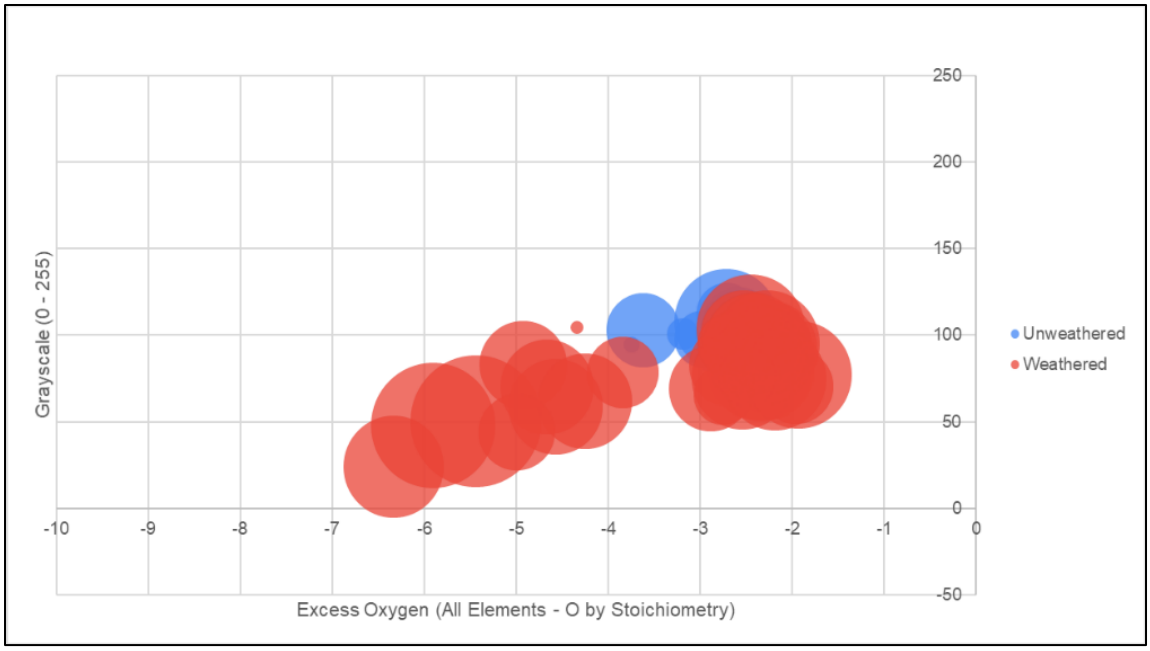

Figure 9: Oxidized and unoxidized measurements plot on top of each other, though oxidized data have more variation on both axes. Bubble size corresponds to proximity to a total of 100; smaller bubbles represent less reliable data.

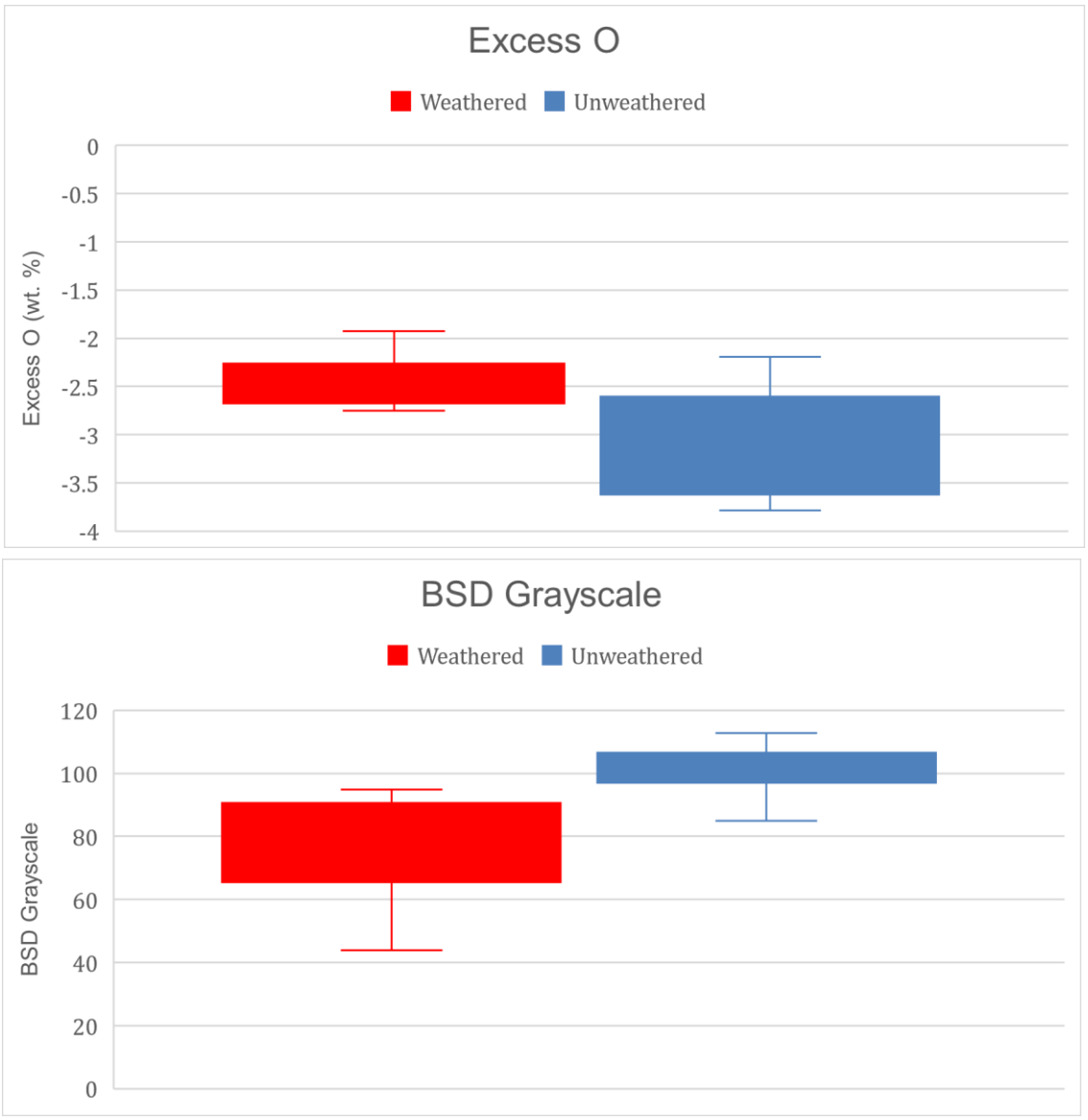

Figure 10: Box-and-whisker plots showing distributions of grayscale and excess O in both oxidized and unoxidized datasets. Two-mean t-tests provide p-values of 0.3452 and 0.00001257, suggesting there is no significant difference between the mean excess O values, but there is between mean BSD grayscale at the α=0.5 significance level. BSD differences are interpreted to be due to compositional differences between oxidized and unoxidized samples, but could also be due to BSD amplifier drift or unintentional changes to instrument settings during SEM session.

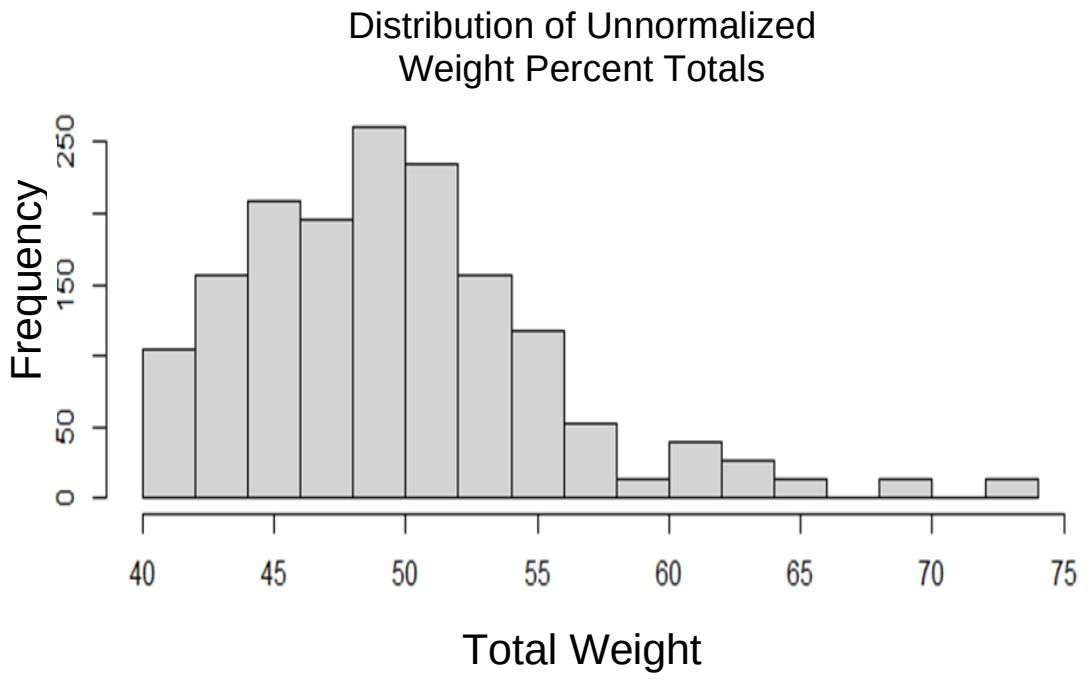

Figure 11: Histogram showing the distribution of unnormalized totals from SEM EDX analysis of glass shards. Totals were lower than hoped as a result of rough shard surfaces following polishing. Data can be found in Appendix C-2.

4.1.2 Glass Shard Composition

Initial results from SEM EDX compositional analysis of prepared glass shards shows that unnormalized totals were low (Appendix C-2). Data analyses were completed using the programming language R. The low totals are the result of rough shard surfaces, which persisted despite careful polishing. Figure 11 shows the distribution of totals. Some measured element wt. % values (e.g., Si, K) are inconsistent with established compositions for the RST (Streck, 1994), casting further doubt over the quality of these analyses.

TC/EA analyses revealed significant variation in measured δD values (range of 45‰). The spatial distribution of these results shows a general decrease in δD moving towards the proposed eruptive center. Streck (1994) describes patterns in outcrop thickness and presence of various flow units related to proximity to the proposed eruptive center, with outcrops of the RST generally thinning at greater distances from the center. To clarify the relationship between isotopic composition and primary characteristics such as texture and shard composition, the SEM was used to collect elemental data from glass shards that underwent preparation for TC/EA analysis.

The results of the SEM EDX analysis reveal compositional variations across glass shards. This is expected, as the RST is known for banding indicating variations in composition. Clear differences in compositions are visible in the boxplots (Figure 12). The results of the ANOVA analyses (Table 1) show significant differences in composition between glass shards. Sample MT-13c is most frequently statistically different by this metric. Some elements, such as Mg, Ti, and Ca, vary considerably but account for a very small wt. % of each sample. Major elements (Si, O, K, Al, Fe, Na) show less significant variation.

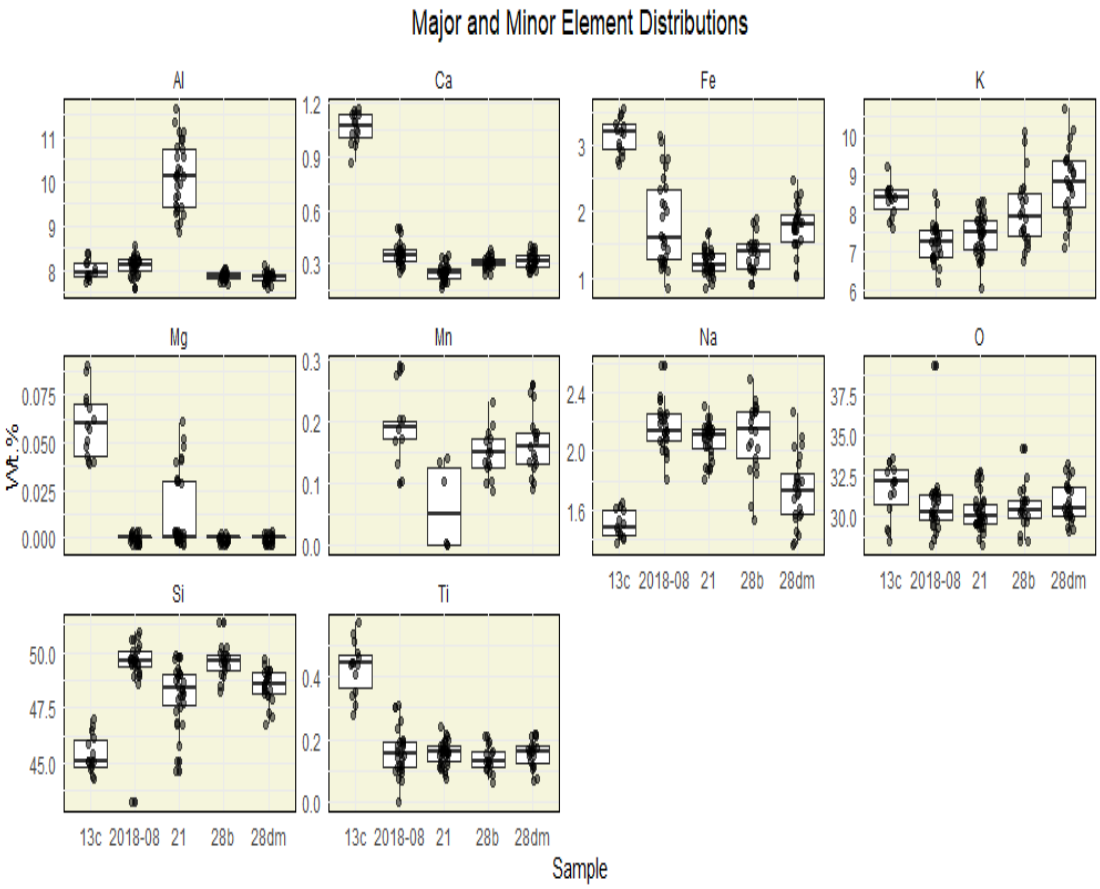

Figure 12: Boxplots showing distributions of elements in glass shards. Outliers were removed to better display interquartile distribution, but were included in ANOVA analyses.

Table 1: Results of ANOVA analyses. Bolded relationships indicate significantly different populations. Relationships were considered significant at a p-value of 0.05. T1: RST2018-08, T2: MT-13c, T3: MT-28dm, T4: MT-28b, T5:MT-21.

Al	Q	p	Ca	Q	p	Fe	Q	p
T1:T2	0.38	0.99889	**T1:T2**	**28.84**	**0**	**T1:T2**	**13.66**	**0**
T1:T3	0.29	0.99961	T1:T3	2.57	0.37025	T1:T3	0.56	0.99464
T1:T4	1.61	0.78553	**T1:T4**	**4.67**	**0.01108**	**T1:T4**	**6.68**	**0.00006**
T1:T5	**4.62**	**0.01215**	**T1:T5**	**4.4**	**0.01948**	**T1:T5**	**6.72**	**0.00006**
T2:T3	0.66	0.9899	**T2:T3**	**31.4**	**0**	**T2:T3**	**14.23**	**0**
T2:T4	1.99	0.62587	**T2:T4**	**33.5**	**0**	**T2:T4**	**20.34**	**0**
T2:T5	**4.25**	**0.02661**	**T2:T5**	**33.24**	**0**	**T2:T5**	**20.38**	**0**
T3:T4	1.32	0.88274	T3:T4	2.1	0.57469	**T3:T4**	**6.11**	**0.00031**
T3:T5	**4.91**	**0.00638**	T3:T5	1.83	0.69362	**T3:T5**	**6.16**	**0.00028**
T4:T5	**6.23**	**0.00022**	T4:T5	0.27	0.99972	**T4:T5**	**0.04**	**0**
Na	Q	p	O	Q	p	Si	Q	p
T1:T2	**7.13**	**0.00002**	T1:T2	0.7	0.98779	T1:T2	1.89	0.66953
T1:T3	**4.25**	**0.02627**	T1:T3	0.21	0.99989	T1:T3	0.32	0.99943
T1:T4	**4.17**	**0.0312**	**T1:T4**	**3.93**	**0.04877**	T1:T4	2	0.62171
T1:T5	1.37	0.86741	T1:T5	0.55	0.99496	T1:T5	1.45	0.84239
T2:T3	2.87	0.25752	T2:T3	0.91	0.96796	T2:T3	1.57	0.8002
T2:T4	2.96	0.23009	**T2:T4**	**4.63**	**0.01193**	T2:T4	3.88	0.05318
T2:T5	**5.75**	**0.00081**	T2:T5	1.25	0.90169	T2:T5	0.44	0.998
T3:T4	**0.09**	**0**	T3:T4	3.72	0.07091	T3:T4	2.31	0.47795
T3:T5	2.88	0.25572	T3:T5	0.35	0.9993	T3:T5	1.14	0.92929
T4:T5	2.79	0.28502	T4:T5	3.38	0.1257	T4:T5	3.45	0.11248
Ti	Q	p	K	Q	p	Mg	Q	p
T1:T2	**18.14**	**0**	T1:T2	3.53	0.09834	T1:T2	0.27	0.99971
T1:T3	1.75	0.7287	**T1:T3**	**4.89**	**0.00675**	**T1:T3**	**0.02**	**0**
T1:T4	0.97	0.95954	T1:T4	1.41	0.85476	T1:T4	2.18	0.53932
T1:T5	1.28	0.89479	T1:T5	0.19	0.99993	**T1:T5**	**0.01**	**0**
T2:T3	**19.89**	**0**	T2:T3	1.36	0.87295	T2:T3	0.29	0.99962
T2:T4	**19.11**	**0**	**T2:T4**	**4.95**	**0.00589**	T2:T4	1.91	0.6603
T2:T5	**19.42**	**0**	T2:T5	3.34	0.13244	T2:T5	0.25	0.99977
T3:T4	0.78	0.98112	**T3:T4**	**6.3**	**0.00018**	T3:T4	2.2	0.53005
T3:T5	0.47	0.99725	**T3:T5**	**4.7**	**0.01025**	**T3:T5**	**0.03**	**0**
T4:T5	0.31	0.99947	T4:T5	1.6	0.78916	T4:T5	2.16	0.54542

4.2 TC/EA Results

δD values are highly varied, with δD_{glass} values ranging from -182‰ to -137‰. Water content of the glasses ranged from 2.7 to 5.1 wt. % H_2O. Carlson (2018) reports an average wt. % H_2O of 2.95 for the Rattlesnake Tuff across two samples, within the range of new data presented here.

Samples MT-28d and MT-28dm, as well as samples MT-28b and MT-28bm, have nearly identical δD values despite being nonmagnetic and magnetic (respectively) (Table 2). Thus, the presence of magnetic components does not appear to impact isotopic composition.

I created isoscapes (Figure 5, Figure 13) to show how δD values are distributed spatially. The modern δD record shows deuterium depletion (decreasing) towards the northeast, with the most positive δD values in the southwest. In the ancient record, the lowest δD values are concentrated in the center of the study area, notably close to the inferred eruptive center of the Rattlesnake Tuff from Streck and Grunder (1997).

There are significantly different patterns between modern and ancient δD values when comparing longitudinal trends (Figure 14). Eastward, deuterium depletion in 7 Ma volcanic glass occurs at nearly four times the rate in the modern system. Results also show no significant relationship between ancient δD and modern elevation ($R^2 = 0.09$), while there is a relationship between modern δD and modern elevation ($R^2 = 0.34$) (Figure 5).

Table 2: Table summarizing isotopic analyses. Sample CVG038 is from Carlson (2018). Samples beginning with "RST" were collected by Carlson and Bershaw in 2018, but prepared by me for this work. Sample MT-14b (starred) is interpreted to be an older than Devine Canyon nonwelded tuff.

Sample	δD_{glass}	δD_{Water}	Wt. % H_2O	Depositional Environment	Hydration water	Latitude	Longitude
MT-13c	-169	-140	5.1	Ash Fall	Precipitation, Fluvial	42.9839	-118.8731
MT-14b*	-166	-138	2.9	Ash Flow	Precipitation, Fluvial	43.0258	-118.63633
MT-19	-140	-111	3.4	Ash Flow	Precipitation, Fluvial	42.8404	-119.66862
MT-20	-151	-122	2.9	Ash Flow	Precipitation, Fluvial	42.8596	-119.74695
MT-21	-137	-107	3.1	Ash Flow	Precipitation, Fluvial	42.7868	-120.2242
MT-23	-149	-120	2.9	Ash Flow	Precipitation, Fluvial	43.9135	-120.30725
MT-24b	-175	-147	3	Ash Flow	Precipitation, Fluvial	43.7829	-119.45026
MT-25	-147	-118	2.8	Ash Flow	Precipitation, Fluvial	43.7525	-119.00905
MT-28a	-178	-150	3.2	Ash Fall	Precipitation, Fluvial	43.6593	-118.99916
MT-28b	-182	-154	2.8	Ash Flow	Precipitation, Fluvial	43.6593	-118.99916
MT-28bm	-182	-154	2.7	Ash Flow	Precipitation, Fluvial	43.6593	-118.99916
MT-28d	-181	-153	2.7	Ash Flow	Precipitation, Fluvial	43.6593	-118.99916
MT-28dm	-181	-153	2.7	Ash Flow	Precipitation, Fluvial	43.6593	-118.99916
RST2018_08	-173	-145	2.9	Ash Flow	Precipitation, Fluvial	43.7096	-119.6356
RST2018_11	-156	-128	2.7	Ash Flow	Precipitation, Fluvial	43.0922	-119.93541
RST2018_18	-158	-129	3.9	Ash Flow	Precipitation, Fluvial	44.4082	-118.98748
M2-CVG038	-146	-117	2.9	Ash flow	Precipitation, fluvial	44.5212	-119.63343

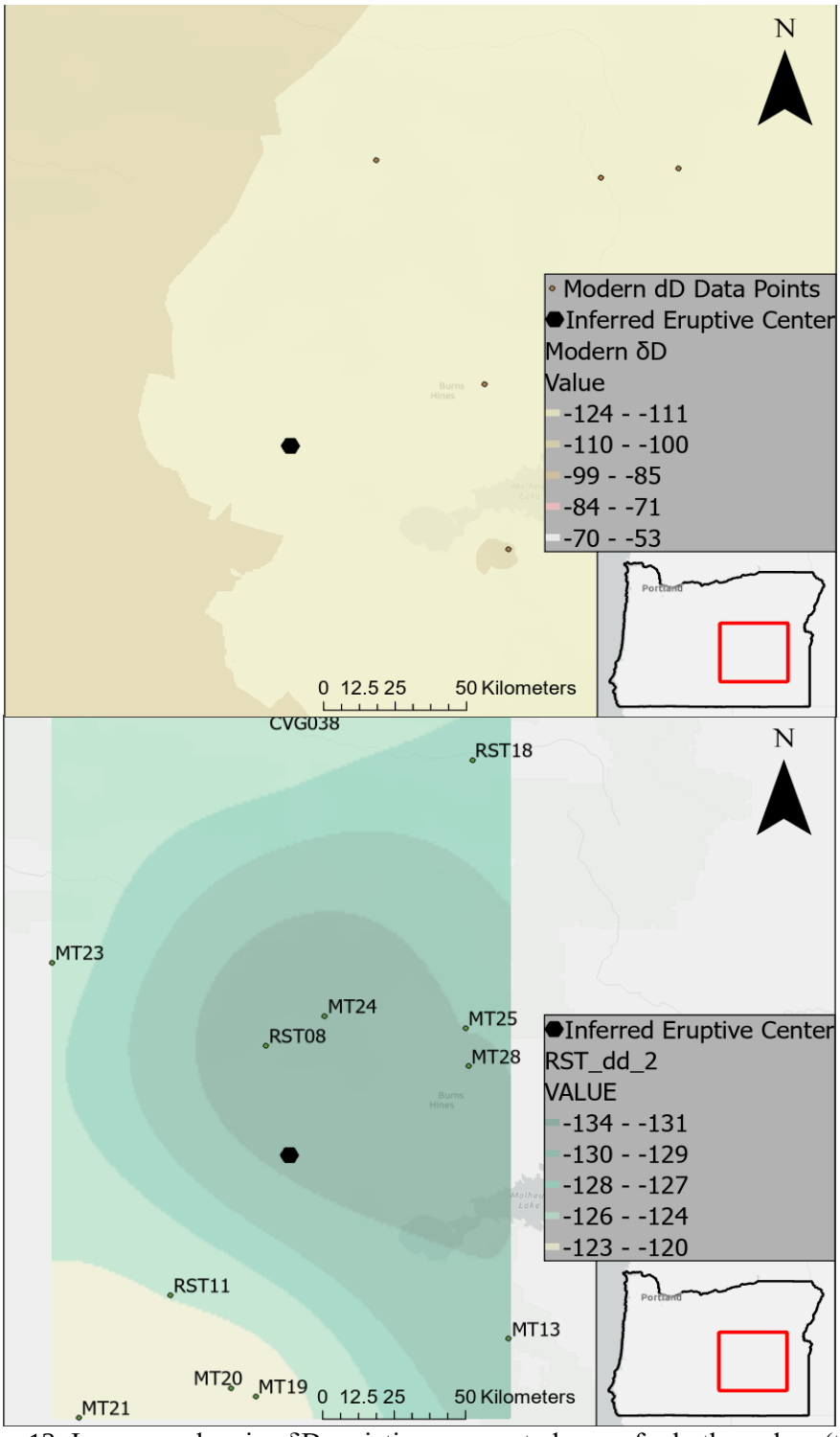

Figure 13: Isoscapes showing δD variation across study area for both modern (top) and ca. 7 Ma (bottom) systems. The inferred eruptive center is shown with the black hexagon.

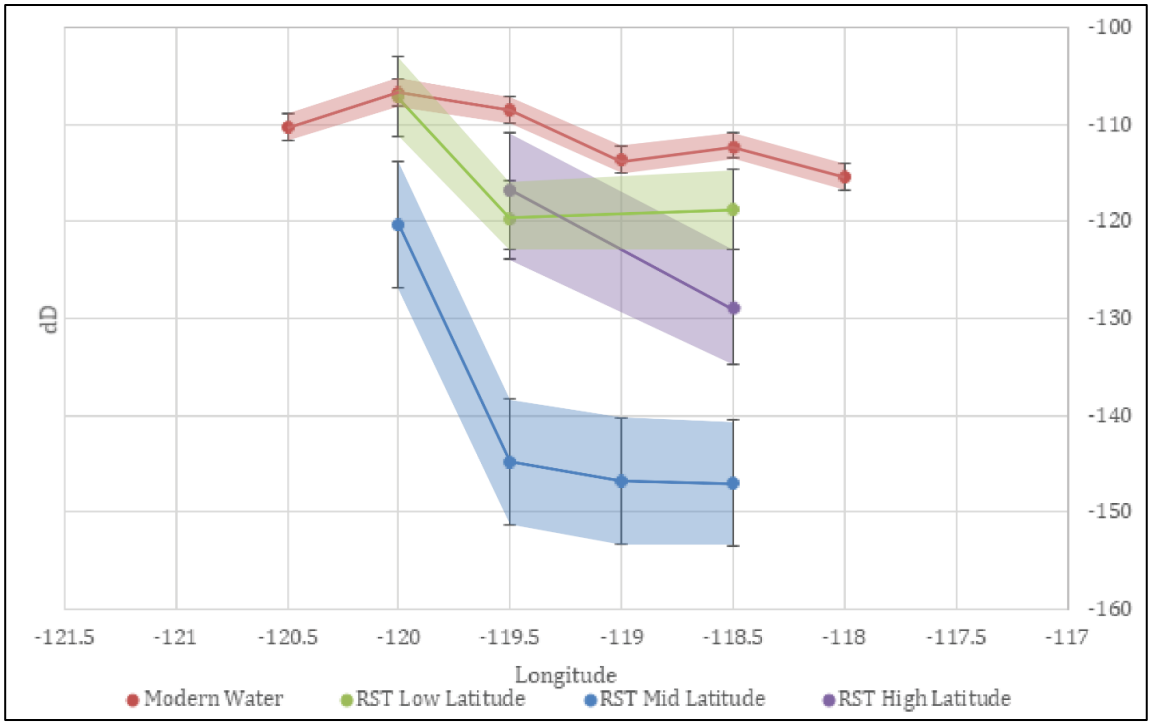

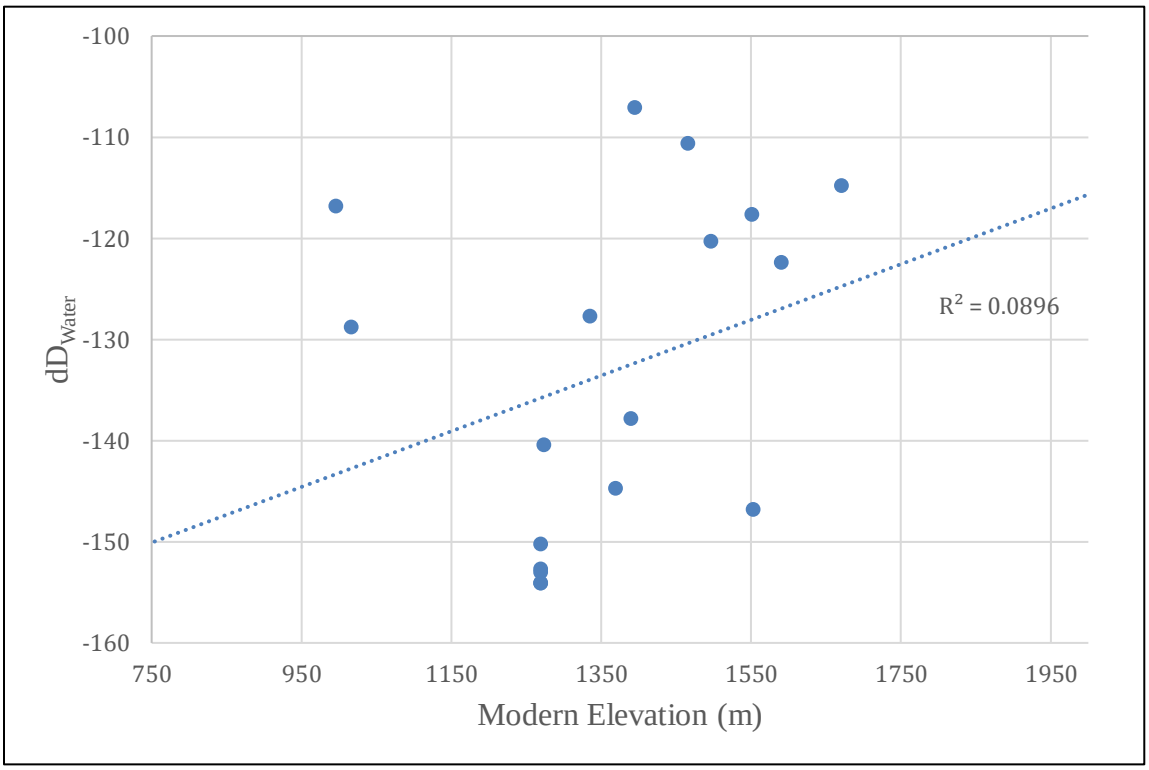

Figure 14: Scatterplots displaying potentially important trends in δD data (or lack thereof). The top scatterplot bins δD by each half degree of longitude and plots averages from each bin. Error bars represent 1 SD of error. The bottom scatterplot highlights the absence of a significant relationship between RST-derived δD and modern elevation

5.0 Discussion

5.1 Effects of Oxidation and Surface Mineralization on the Passivating Layer

Though initial backscatter imaging suggested that there were significant chemical differences between oxidized and unoxidized tuff, the subsequent data collected does not support this hypothesis. In particular, the data support the finding that excess O, and by extension water, is approximately equally abundant in both tuff populations. A T-test statistic of 0.3452 confirms that there is no significant difference between the excess O in each tuff. However, there is a significant difference in grayscale (p test statistic of 0.00001257) assuming no detector amplifier drift. From this, I conclude that while the average Z between oxidized and unoxidized tuff is significantly different, it is not a result of differences in water content. Within the context of my thesis work, this finding is critically important, as it confirms that glass that is suitable by optical standards is chemically suitable for isotopic analysis.

To explore differences in average Z between oxidized and unoxidized tuffs, I conducted 2-mean t-tests comparing concentrations of 6 elements involved in hydration through cation exchange (Fe, Na, Ca, K, Al, and Si) between populations. The results of these tests found no significant differences between oxidized and unoxidized populations. Thus, the measured grayscale differences remain statistically unexplained. I suggest that the gradients in the preliminary images are not representative of actual Z gradients within shards, but rather an irregular sample surface.

5.2 Effects of Glass Shard Composition on Water Content and δD

Here, I assess the relationship between composition and the stable isotopic and water content of the shards. SEM EDX data show that glass shards have variable composition. It is important to recognize that these data have significant error associated with them. Typically, wt. % calculated from EDX analyses have an associated 3σ range of +/- 0.5 wt. %. However, analysis of samples with rougher surfaces that produce very low wt. % totals likely have significantly more error, though this hasn't been well constrained. In my data, this is reflected in some wt. % values being ~2-3% different than established RST compositions (e.g. Streck 1994). Therefore, I emphasize that compositional data presented is qualitative at best, and does not represent actual elemental concentrations in treated glass shards. Sample MT-13c is of particular interest because it shows significantly different wt. % measurements in Ca, Fe, and Na and has an anomalously high wt. % H_2O as measured during TC/EA analysis (5.1%). To assess the relationship between composition and wt. % H_2O, regression analyses were done for each element (Figures 15 and 16). From this, we see that there are significant relationships between some elemental concentrations and wt. % H_2O. More specifically, for the five samples analyzed, elements most associated with changes in Wt. % H_2O are Mg (R^2 = 1.00), Ca (R^2 = 0.96), Ti (R^2 = 0.98), Mn (R^2 = 0.71), and Fe (R^2 = 0.78). However, the results of the TC/EA analysis (Wt. % H_2O ranging from 2.7 – 5.1) are typical of normally hydrated glasses, and do not suggest mineral contamination. Additionally, SEM imaging of prepared glass shards revealed no mineral contaminants on the surface or as microlites within the shards themselves. Though R^2 values suggest highly significant relationships between composition and wt. % H_2O, I believe that this is an inappropriate metric. In

many cases, a single outlier (typically sample MT-13c, which has the highest wt. % H_2O), defines such high R^2 values. Without this outlier, there is little relationship between wt. % H_2O and elemental abundance. Removing this sample (MT-13c) from the distribution gives revised correlations with wt. % H_2O of Mg ($R^2 = 0.97$), Ca ($R^2 = 0.03$), Ti ($R^2 = 0.08$), Mn ($R^2 = 0.43$), and Fe ($R^2 = 0.23$). These relationships fail to assess other important factors that we know are influential on glass hydration, such as depth beneath the ground surface (Carlson, 2018; Jimenez-Rodriguez et al., 2023).

In addition, there is no significant relationship between δD and wt. % H_2O, suggesting that glass shard composition plays no role in the rehydration by meteoric water. Past work has shown that diffusion of meteoric water into volcanic glass causes hydrogen exchange and can release ions (Na^+, K^+, Rb^+, Ca^{2+}, Mg^{2+}) (Cassel and Breecker, 2017; Jimenez-Rodriguez et al., 2023). These compositional changes occur as a result of secondary hydration, but do not control it. This could explain some of the observed correlation between wt. % H_2O and element composition, but previous concerns about R^2 values being skewed by outliers remain. Thus, for this dataset, I suggest that R^2 values are insufficient to determine whether there is a relationship, and that factors other than composition may be responsible for variations in water content.

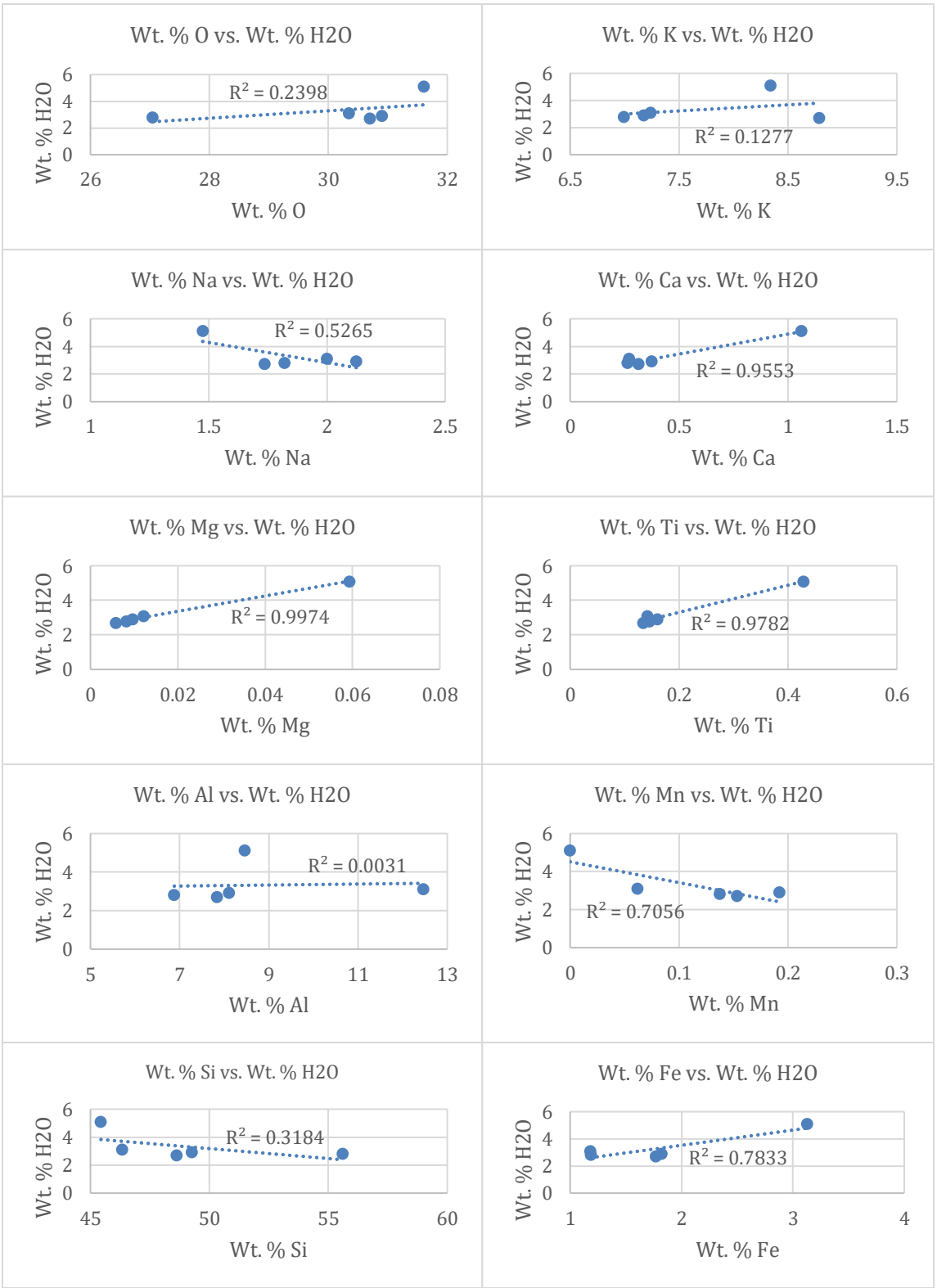

Figure 15: Graphs displaying linear regression analyses examining relationships between element and water concentrations.

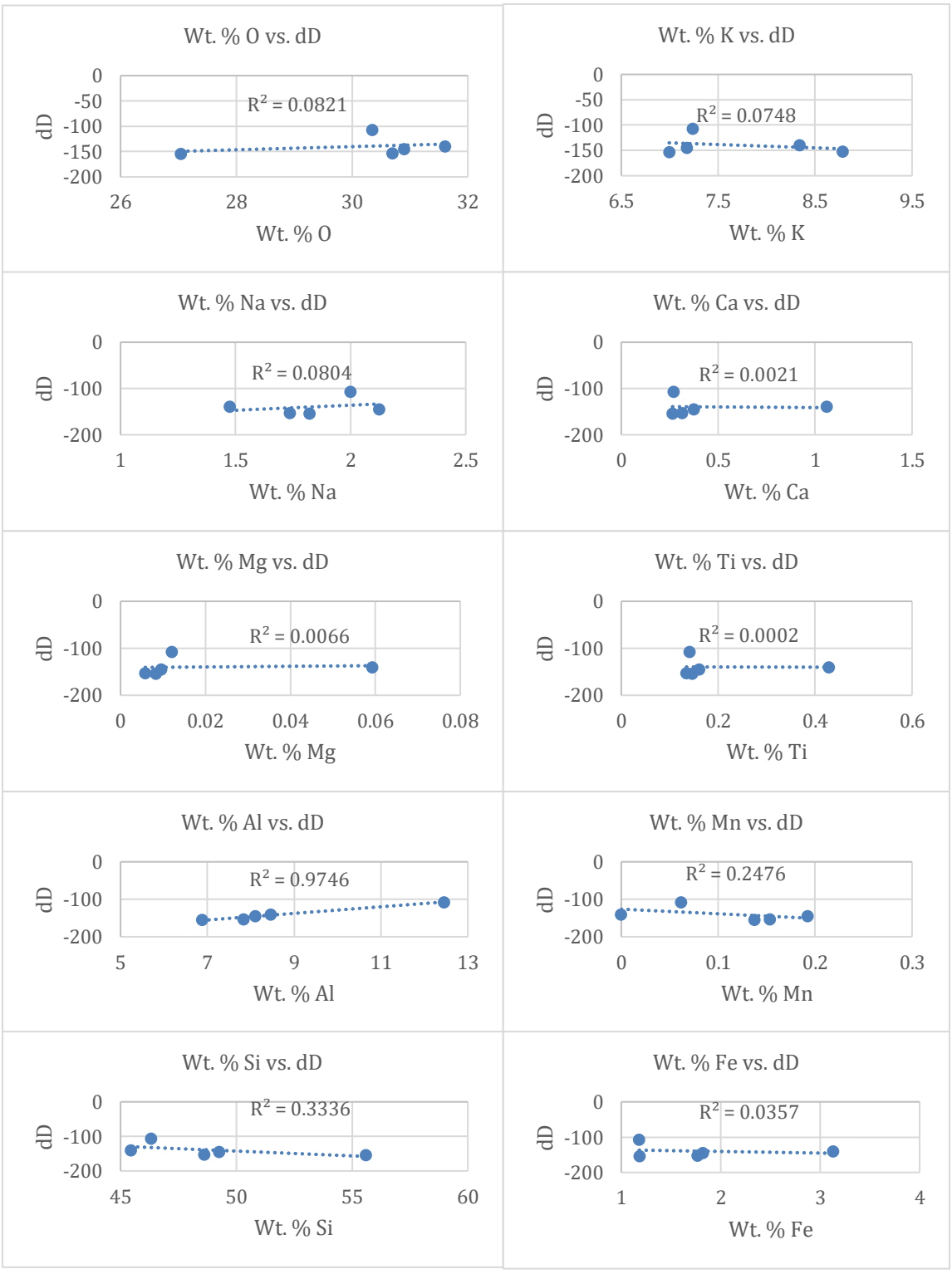

Figure 16: Graphs displaying linear regression analyses examining relationships between δD and elemental concentrations. Importantly, many displayed R^2 values are defined by a single outlier, and are interpreted to be largely meaningless.

An additional set of regression analyses were performed to assess the relationship between elemental composition and δD. Though there is evidence to suggest analyzed water was derived only from pristine glass (Figure 17), significant relationships between elemental composition and δD would suggest that secondary minerals containing modern, isotopically distinct water may be present. Based on the results of a regression analyses (Figure 16), only one element (Al, $R^2 = 0.97$) has a statistically significant relationship with δD. Looking more closely at the relationship, we see that four out of five samples have very similar Al concentrations, while one (MT-21) is a statistical outlier. This causes the relationship between wt. % Al and δD to appear more significant than it is. MT-21 has a non-remarkable amount of water (3.1 wt. % H_2O), but is notable for having

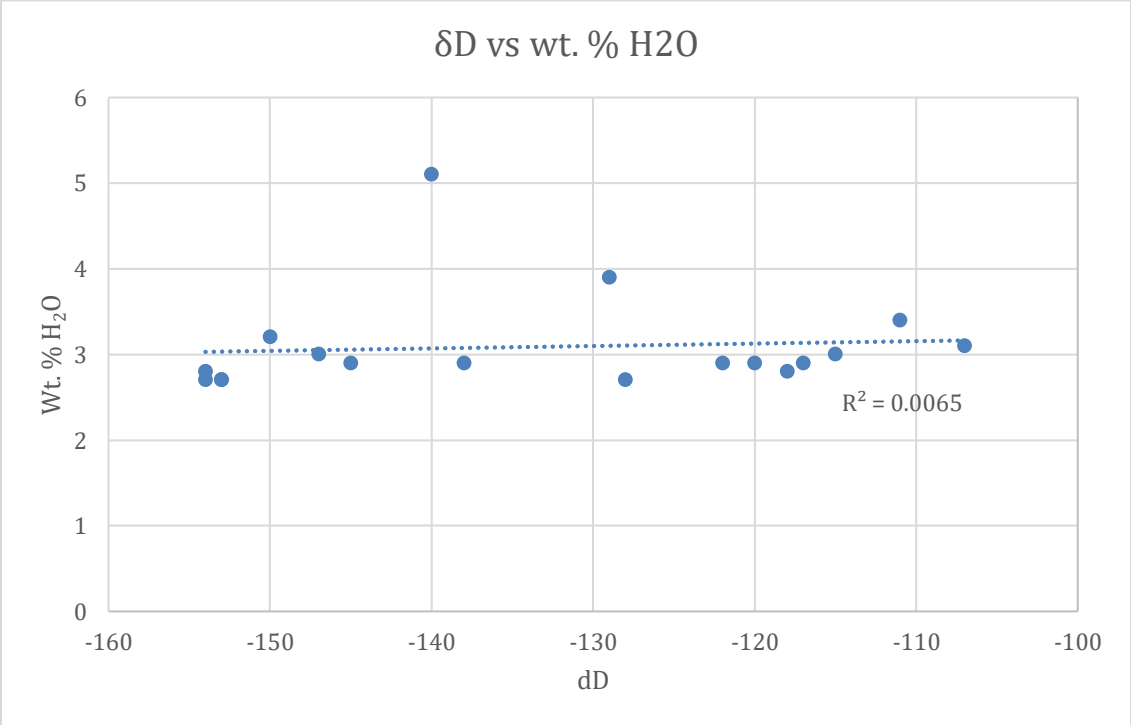

Figure 17: Graph showing no relationship between δD and wt. % H_2O. This indicates there is no magmatic water influence on δD values. If there were a strong negative correlation between the variables, one could conclude that the additional water raises δD. Magmatic water has less negative δD.

the highest δD of all analyzed samples (-107‰). Other than its longitude (furthest sample to the west), there is no clear cause for its relatively high δD value. Its poor sorting and the presence of angular pumice clasts suggest deposition in an ash flow, which is consistent with other samples. Thus, I conclude that though glass shards contain variable compositions, this does not result in differences in wt. % H_2O or δD.

5.3 Effect of Magmatic Water on Water Content and δD

Magmatic δD values are typically much less depleted in deuterium relative to those measured (roughly -40‰ - -80‰) (Seligman et al., 2016; Befus et al., 2020). Thus, δD values measured closer to the inferred eruptive center would likely show higher (less negative) δD values, as glasses in thicker cooling units have the potential to be rehydrated by degassed magmatic water sourced from deeper in the unit (Seligman et al., 2016). In addition, deeper glasses have the potential to receive less hydration by meteoric water, and can have a higher proportion of primary magmatic water compared to shallower deposits. These scenarios are inconsistent with the observation that relatively depleted δD values are centered around the inferred eruptive center of the RST (Figure 13). Highly explosive eruptions such as the RST have been shown to retain between 0.2 and 0.6 wt. % magmatic water, suggesting that well-hydrated glasses such as those in this study contain a majority meteoric water (Giachetti et al., 2015; Seligman et al., 2016). Additionally, a significant relationship between δD and wt. % H_2O is commonly viewed as a metric for magmatic water influence. There is no statistically significant relationship between these variables (Figure 17). The opposite is observed, so I suggest magmatic water plays no significant role in measured δD values.

5.4 Paleoenvironmental Interpretations

The lack of a meaningful correlation between modern elevation and δD values measured from ancient (7 Ma) glass strengthens the assumption that well prepared volcanic glass produces δD values that reflect ancient meteoric water, as modern δD values do show variations in response to modern elevation (Figure 5, Figure 13). This is further supported by the fact that spatial trends visible in the modern isoscape do not match those in the ancient isoscape ~7 Ma (Figure 13).

While deuterium isotopes at both times become depleted (decrease in δD value) to the east, the magnitude of depletion in the paleoisoscape is much higher. Over the same distance from west-east (approximately 200km), deuterium is depleted nearly four times more in the ancient system as compared to modern (Figures 13 and 14). I also observe that the lowest δD values are largely clustered in and around the eruptive center of the Rattlesnake Tuff proposed by Streck and Grunder (1997). To assess the paleoenvironmental conditions responsible for this trend, I employ the framework of the three previously discussed isotopic controls: the amount, altitude, and continental effects (Figure 5).

5.4.1 Cascade Topographic Barrier

The difference in the modern and 7 Ma isoscape is unlikely to be due to changes in Cascade elevation because just east of the range at approximately -120º longitude, modern and ancient δD values are nearly identical (Figure 14). I interpret this to mean that the Cascades and other topographic features to the west (the Oregon Coast Range) were likely at similar elevations in the late Miocene (~Ma) compared to today.

5.4.2 The Amount Effect

Central Oregon today is characteristically dry and receives sporadic precipitation (Figure 2). Relationships between modern precipitation amounts and modern δD suggest the amount effect does not play a significant role in trends of δD values in central Oregon (Figure 5). Hydration of volcanic glass can be heavily influenced by outcrop thickness and the formation of smectites in volcanic soils. Smectites swell when hydrated and can prevent glasses beneath them from hydrating in all but the heaviest precipitation events (Jimenez-Rodriguez et al., 2023). Thus, volcanic glass may more completely record heavy precipitation, which can infiltrate through smectite barriers. Today, central Oregon receives some of its annual rainfall through summer and fall convective storms (Ochoa et al., 2018). These large, heavy rainfall events lift large amounts of moisture high into the atmosphere, where lower temperatures and a relatively humid air column result in precipitation with lower δD values (Risi et al., 2023). This has potential to overprint isotopic patterns produced by topographic features (Rohrmann et al., 2014). If the amount effect (convective thunderstorms) were more significant ca. 7 Ma, one might expect it to affect all of central and eastern Oregon, resulting in a much more uniform distribution of relatively low δD values. This is inconsistent with my results, suggesting that an enhanced amount effect was not the cause of observed patterns in δD ~7 Ma.

5.4.3 The Continental Effect

The continental effect accounts for the majority of the decreasing δD trend across central and eastern Oregon today (Figure 5). However, the pattern in δD values ~7 Ma (Figure 13) shows a localized depletion just north of the modern-day Harney Basin. The

continental effect generally causes depletion in a more uniform pattern than is observed, which is inconsistent with the anomaly.

5.4.4 The Altitude Effect

In modern central Oregon, the altitude effect accounts for a significant portion of localized variation in δD (Figure 5). Areas such as the Blue Mountains in northeastern Oregon and other isolated peaks feature localized depletions in δD associated with their elevation (Figure 13). δD values derived from the RST present a similarly local pattern of more negative δD centered north the Harney Basin, which is its inferred eruptive center (Streck, 1994) (Figure 13). The pattern seen in Figure 13 is consistent with δD depletion due to an isolated topographic high, such as a volcanic edifice.

5.4.5 Lapse Rates and Elevation Estimates

Considering that the lowest δD values in the paleoisoscape are concentrated around the eruptive center inferred by Streck and Grunder (1997), I propose that the region that is now located near the junction of routes 395 and 20, west-northwest of the Harney Basin, contained a significant topographic feature ~7 Ma. This interpretation is consistent with trends observed in modern meteoric water (Figure 13), where the Blue Mountains in NE Oregon and peaks around Newberry Crater in central Oregon cause localized decreases in meteoric water δD. The change in elevation between Bend, Oregon and the top of Newberry Crater is approximately 900m. The associated change in δD is ~-11‰ (-110‰ in Bend and -121‰ at the peak) (Lesley Chesson, 2016; USGS, 2019) or -12.2‰/km. An isotopic lapse rate for the Ochoco Mountains has been established for δD of -26.4‰/km of altitude (Greenwood, pers. comm. 2023). This isotopic lapse rate is

steeper than that observed on the western side of the Cascades, which is -20.6‰/km (Brooks et al., 2012). Estimating paleoelevation based on modern -26.4‰/km and -12.2‰/km lapse rates and a decrease in δD of -35‰ ~7 Ma, a topographic feature between 1.3 km and 2.8 km in elevation would have existed near the inferred eruptive center ca. 7 Ma.

Interestingly, the RST exists today as a widespread, mostly flat-lying ash flow tuff. There is little variation in unit thickness, with beds thickening slightly towards the inferred eruptive center (Streck & Grunder, 1995). There are no known outcrops of the RST immediately around the eruptive center (Figure 1). However, previous work indicates that this was not always the case. Around the inferred eruptive center, there are no RST outcrops because it is overlain by younger basalt deposits (Streck and Grunder, 2012). Today's flat-lying, horizontally continuous RST outcrops suggest that the landscape in areas currently covered with RST were flat lying ca. 7 Ma (Streck, 1994). This is because despite appearing on ridgetops and valley floors, thickness variations in RST outcrops are quite small (tens of meters) (Streck & Grunder, 1995). The RST contains large, imbricated clasts (pumice and other lithics) throughout, indicating a high-energy ash flow depositional environment. The flat-lying nature of today's RST outcrops suggests that any topographic features associated with HLP volcanism in or near Harney Basin was very localized. Today's RST outcrops show no evidence of significant tectonic deformation (Streck, 1994). During the late Miocene, the Harney Basin and surrounding areas was volcanically active, with many silicic domes and ash-flow tuffs erupting from the region during this time (Greene et al., 1972; Streck, 1994; Walker, 1970). Thus, it

seems plausible that significant topographic features could have existed, that have since eroded away.

There are other topographic features in the Cascade rain shadow that cause δD gradients now and in the past. Kukla et al. (2020) describe similar isotopic patterns in the Blue Mountains, suggesting elevation and precipitation seasonality have contributed to isotopic trends for nearly 50 million years. They conclude that local topographic features within the rain shadow of the Cascades can have significant impacts on local flora and fauna, as well as on isotopic patterns, but that paleotopography throughout central and eastern Oregon is poorly constrained. My results suggest that in addition to the existence of ancient topography associated with the Blue Mountains, volcanic edifices, like the RST silicic dome, existed in the past and have since been eroded away. The timescale for the destruction of the proposed feature is

5.4.6 Hypotheses for Topography

In addition to δD evidence for topography, there are also features in outcrops of around the inferred eruptive center that support this interpretation. First, RST outcrops are thickest ~30-40km from the inferred eruptive center, and thin both towards and away

from these thickest areas (Figure 18) (Streck and Grunder, 1995). Thinning towards the eruptive center is consistent with deposition on the flanks of some topographic feature.

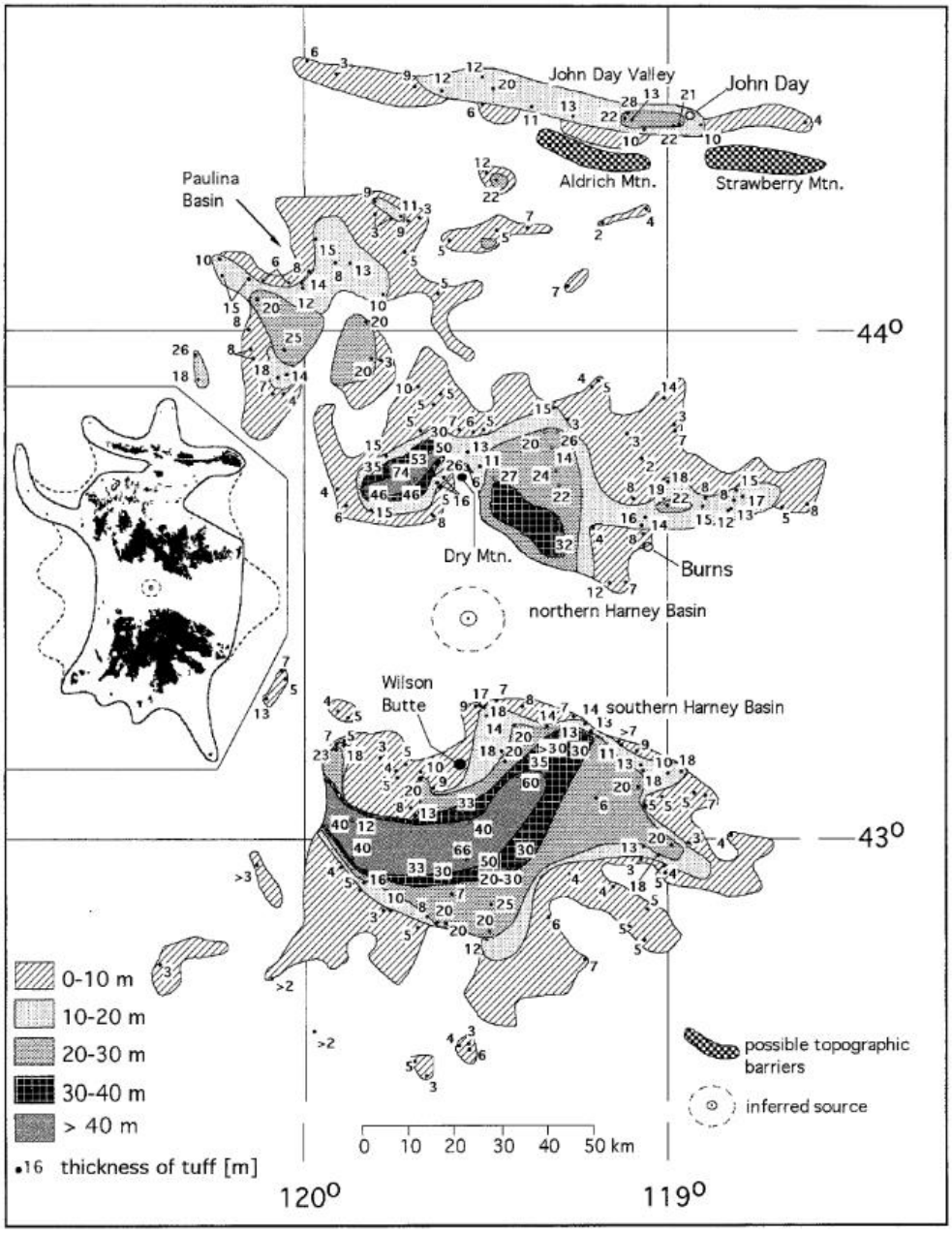

Figure 18: Isopach map of the Rattlesnake Tuff from Streck and Grunder (1995). Note thickest outcrops are not closest to eruptive center; tuff thins towards eruptive center.

Additionally, basalts overlying the RST in the western Harney Basin (the location of the inferred eruptive center) do so unconformably, suggesting millions of years of non-deposition on top of the RST nearest the eruptive center (Streck and Grunder, 2012). This can be explained by topography.

5.4.6.1 Lava Domes

There have been few eruptions like the RST in recent times. However, the Novarupta-Katmai eruption in Alaska in 1912 has many similarities to the RST. The eruption took place over ~60 hours and expelled 13-14km^3 of magma from a zoned chamber (Hildreth and Fierstein, 2012). It is a part of the volcanically active Valley of Ten-Thousand Smokes (VTTS) region, which features many volcanic edifices of varying heights, ranging from 65m (the product of the Novarupta eruption) to 2330m (Hildreth and Fierstein, 2012). The VTTS is similar to the HLP in that it lies in a back-arc setting. Modern analogs like this reveal that volcanically active regions that produce large, voluminous rhyolitic eruptions do create significant topographic features, as I conclude for the RST in Central Oregon.

The Chaitén Volcano in Chile is another modern analog for caldera-producing rhyolitic eruptions. The last major eruption of Chaitén was ~10000 years ago, which resulted in a caldera collapse and subsequent effusive construction of a large lava dome ~400m high (Carn et al., 2009). The dome is estimated to be ~5600 years old and is part of a feature with a total relief of ~850m.

The VTTS is heavily impacted by heavy glaciation during the winter, which contributes to relatively high erosion rates. This is especially true for ash and pumice

deposits, which are relatively underrepresented in the volcanic record because they are more easily eroded than lava flows (Fierstein and Hildreth, 2000). Areas of higher elevation in central and eastern Oregon have been covered with glaciers multiple times since the emplacement of the RST. The Wallowa mountains of northeastern Oregon show evidence of at least three glaciations since just ~25 ka (Licciardi et al., 2004). This suggests that high topography produced by HLP volcanism could have been subject to similar glaciation. Thus, I suggest that the RST and other late-Miocene HLP eruptions could have produced topography equivalent to or greater than that currently in the VTTS and Chaitén, and that such landscapes are subject to rapid erosion through glaciation or other means, explaining the modern-day absence of topography in the Harney Basin region.

5.4.6.2 Resurgent Domes

Resurgent domes are another type of topographic feature associated with large caldera-forming eruptions (Bailey et al., 1976). These features result from the mechanical uplift of the collapsed caldera floor by magma refilling the underlying chamber post-eruption (Smith and Bailey, 1968). These features are somewhat common in large calderas formed by eruptions of widespread ignimbrites (Long Valley Caldera, CA; Valles Caldera, NM), and are known to produce variable topography ranging from ~100m (Bailey et al., 1976) to in excess of 1 km (Goff et al., 2006). Uplift rates for these features seem to be variable, though there is evidence in the Long Valley Caldera for uplift to have ceased by ~100 thousand years post-eruption (Bailey et al., 1976). Resurgent domes are typically 10s of kilometers across and their uplift is often

accommodated by ring fractures (which also serve as conduits for subsequent eruptions (Bailey et al., 1976). These features may subside once regional magmatism ceases, providing an interesting mechanism for the proposed topography associated with the RST ~ 7 Ma.

6.0 Conclusion

I present new stable isotopic and compositional data for 16 glass samples collected from the Rattlesnake Tuff in central Oregon. With these data, I show that δD values derived from the ca. 7 Ma RST exhibit anomalously low δD values clustered around their inferred eruptive center. I also show that there are not significant variations in δD within outcrops, even if varied depositional environments are represented. Evaluation of the differences between modern and late Miocene isoscapes motivates questions about primary magmatic water overprint of δD values and the effects of glass shard composition on δD values due to δD depletion being centralized around the inferred eruptive center. Statistical analyses of variations in glass composition show that shards possess statistically different elemental compositions. However, compositional variation is not associated with differences wt. % H_2O or δD. I conclude that the elemental composition of volcanic glass does not affect its ability to incorporate water or the water's stable isotopic composition. I also show that there is no statistically significant relationship between wt. % H_2O and δD, suggesting that the magmatic signal has a negligible effect on hydrated glass δD values. Overall, I conclude that relatively low δD values centered around the inferred RST eruptive center are the result of an isolated topographic feature within the present-day Harney Basin related to High Lava Plains volcanic activity. This is comparable to the modern-day VTTS and Chaitén lava domes, as well as resurgent doming in the Long Valley and Valles Calderas. Using three different δD lapse rates, I estimate paleoelevation of the ca. 7 Ma HLP topographic feature to be 1.3 km to 2.8 km above the present-day ground surface to account for the observed decline in ancient water δD.

Future Work

Following the outcomes of this work, I see clear opportunities for additional research to be done in this space. Possible avenues include:

1. Evaluation of spatial distributions of δD from other mid-late Miocene glasses (Dinner Creek, Devine Canyon) to see if similar trends (lower δD closer to the inferred eruptive center) exist.
2. More thorough analysis of modern water isotope distributions to better characterize controls on spatial variations. This could involve collecting an internally consistent modern water dataset, which I did not have.
3. Stratigraphic and basin analysis of the Harney Basin to further characterize the topography of the region in the late Miocene.

Works Cited

Bailey, R.A., Dalrymple, G.B., and Lanphere, M.A., 1976, Volcanism, structure, and geochronology of Long Valley Caldera, Mono County, California: Journal of Geophysical Research (1896-1977), v. 81, p. 725–744, doi:10.1029/JB081i005p00725.

Bershaw, J., Cassel, E. J., Carlson, T. B., Streig, A. R., & Streck, M. J. (2019). Volcanic glass as a proxy for Cenozoic elevation and climate in the Cascade Mountains, Oregon, USA. *Journal of Volcanology and Geothermal Research*, *381*, 157–167. https://doi.org/10.1016/j.jvolgeores.2019.05.021

Bershaw, J., Hansen, D., & Schauer, A. (2020). Deuterium excess and 17O-excess variability in meteoric water across the Pacific Northwest, USA. Tellus B. https://doi.org/10.1080/16000889.2020.1773722

Bestland, E. A. (1997). Alluvial Terraces and Paleosols as Indicators of Early Oligocene Climate Change (John Day Formation, Oregon). SEPM Journal of Sedimentary Research, Vol. 67. https://doi.org/10.1306/D4268653-2B26-11D7-8648000102C1865D

Befus, K. S., Walowski, K. J., Hervig, R. L., & Cullen, J. T. (2020). Hydrogen Isotope Composition of a Large Silicic Magma Reservoir Preserved in Quartz-Hosted Glass Inclusions of the Bishop Tuff Plinian Eruption. Geochemistry, Geophysics, Geosystems, 21(12), e2020GC009358. https://doi.org/10.1029/2020GC009358

Cahoon, E. B., Streck, M. J., Koppers, A. A. P., & Miggins, D. P. (2020). Reshuffling the Columbia River Basalt chronology—Picture Gorge Basalt, the

earliest- and longest-erupting formation. *Geology*, *48*(4), 348–352. https://doi.org/10.1130/G47122.1

Carlson, T. (2018). *Volcanic Glass as a Paleoenvironmental Proxy: Comparing Preparation Methods on Ashes from the Lee of the Cascade Range in Oregon, USA*. https://doi.org/10.15760/etd.6356

Carn, S.A., Pallister, J.S., Lara, L., Ewert, J.W., Watt, S., Prata, A.J., Thomas, R.J., and Villarosa, G., 2009, The Unexpected Awakening of Chaitén Volcano, Chile: Eos, Transactions American Geophysical Union, v. 90, p. 205–206, doi:10.1029/2009EO240001.

Cassel, E. J., & Breecker, D. O. (2017). Long-term stability of hydrogen isotope ratios in hydrated volcanic glass. *Geochimica et Cosmocimica Acta*, *200*, 67–86. https://doi.org/10.1016/j.gca.2016.12.001.

Caves, J. K., Winnick, M. J., Graham, S. A., Sjostrom, D. J., Mulch, A., & Chamberlain, C. P. (2015). Role of the westerlies in Central Asia climate over the Cenozoic. Earth and Planetary Science Letters, 428, 33–43. https://doi.org/10.1016/j.epsl.2015.07.023

Dansgaard, W. (1964). Stable isotopes in precipitation. Tellus, 16(4), 436–468. https://doi.org/10.1111/j.2153-3490.1964.tb00181.x

Friedman, I., Gleason, J., Sheppard, R. A., & Gude 3rd, A. J. (1993). Deuterium Fractionation as Water Diffuses into Silicic Volcanic Ash. In Climate Change in Continental Isotopic Records (pp. 321–323). American Geophysical Union (AGU). https://doi.org/10.1029/GM078p0321

Friedman, I., Gleason, J., & Warden, A. (1993). Ancient Climate from Deuterium Content of Water in Volcanic Glass. In *Climate Change in Continental Isotopic Records* (pp. 309–319). American Geophysical Union (AGU). https://doi.org/10.1029/GM078p0309

Giachetti, T., Gonnermann, H. M., Gardner, J. E., Shea, T., & Gouldstone, A. (2015). Discriminating secondary from magmatic water in rhyolitic matrix-glass of volcanic pyroclasts using thermogravimetric analysis. Geochimica et Cosmochimica Acta, 148, 457–476. https://doi.org/10.1016/j.gca.2014.10.017

Goff, F., Gardner, J.N., Reneau, S.L., and Goff, C.J., 2006, Geologic map of the Redondo Peak quadrangle, Sandoval County,New Mexico: New Mexico Bureau of Geology and Mineral Resources Open-File Report.

Gonfiantini, R., Roche, M.-A., Olivry, J.-C., Fontes, J.-C., & Zuppi, G. M. (2001). The altitude effect on the isotopic composition of tropical rains. Chemical Geology, 181(1–4), 147–167. https://doi.org/10.1016/S0009-2541(01)00279-0

Greene, R. C., Walker, G. W., & Corcoran, R. E. (1972). Geologic map of the Burns Quadrangle, Oregon [Map]. US Geological Survey. https://ngmdb.usgs.gov/Prodesc/proddesc_9455.htm

Greene, R. C. (1973). *Petrology of the welded tuff of Devine Canyon, Southeastern Oregon* (Professional Paper No. 797; Professional Paper). USGS.

Fierstein, J., & Hildreth, W. (2000). Preliminary Volcano-Hazard Assessment for the Katmai Volcanic Cluster, Alaska (Open-File Report No. 00–489; Open-File Report). United States Geological Survey, Alaska Volcano Observatory.

Hildreth, W., & Fierstein, J. (2012). The Novarupta-Katmai Eruption of 1912—Largest Eruption of the Twentieth Century: Centennial Perspectives (Professional Paper).

Jimenez-Rodriguez, S., Quade, J., Levin, N. E., Campisano, C. J., Stinchcomb, G. E., Roman, D. C., & Bedaso, Z. (2023). Environmental controls on the hydrogen isotopic composition of volcanic glass from the Southern Afar rift, eastern Ethiopia. Chemical Geology, 121484. https://doi.org/10.1016/j.chemgeo.2023.121484

Jordan, B. T., Grunder, A. L., Duncan, R. A., & Deino, A. L. (2004). Geochronology of age-progressive volcanism of the Oregon High Lava Plains: Implications for the plume interpretation of Yellowstone. Journal of Geophysical Research: Solid Earth, 109(B10). https://doi.org/10.1029/2003JB002776

Kohn, M. J., & Law, J. M. (2006). Stable isotope chemistry of fossil bone as a new paleoclimate indicator. *Geochimica et Cosmochimica Acta*, *70*(4), 931–946. https://doi.org/10.1016/j.gca.2005.10.023

Kohn, M. J., Miselis, J. L., & Fremd, T. J. (2002). *Oxygen isotope evidence for progressive uplift of the Cascade Range, Oregon*.

Kukla, T., Ibarra, D. E., Rugenstein, J. K. C., Gooley, J. T., Mullins, C. E., Kramer, S., Moragne, D. Y., & Chamberlain, C. P. (2021). High-Resolution Stable

Isotope Paleotopography of the John Day Region, Oregon, United States. Frontiers in Earth Science, 9, 30. https://doi.org/10.3389/feart.2021.635181

Lee, J. E., & Fung, I. (2008). "Amount effect" of water isotopes and quantitative analysis of post-condensation processes. Hydrological Processes: An International Journal, 22(1), 1-8.

Licciardi, J., Clark, P., Brook, E., Elmore, D., & Sharma, P. (2004). Variable responses of western U.S. glaciers during the last deglaciation. Geology, 32(1), 81–84. https://doi.org/10.1130/G19868.1

McLean, A., & Bershaw, J. (2021). Molecules to Mountains: A Multi-Proxy Investigation Into Ancient Climate and Topography of the Pacific Northwest, USA. *Frontiers in Earth Science*, *9*. https://doi.org/10.3389/feart.2021.624961

Ochoa, C. G., Caruso, P., Ray, G., Deboodt, T., Jarvis, W. T., & Guldan, S. J. (2018). Ecohydrologic Connections in Semiarid Watershed Systems of Central Oregon USA. Water, 10(2), Article 2. https://doi.org/10.3390/w10020181

Poage, M. A., & Chamberlain, C. P. (2001). Empirical relationships between elevation and the stable isotope composition of precipitation and surface waters: considerations for studies of paleoelevation change. American Journal of Science, 301(1), 1-15.

PRISM Climate Group at Oregon State University. (2022). Retrieved February 28, 2022, from https://prism.oregonstate.edu/projects/gallery_view.php?state=OR

Retallack, G. J. (1991). A field guide to mid-Tertiary Paleosols and paleoclimatic changes in the high desert of central Oregon; Part I. *Oregon Geology*, *53*(3), 51.

Retallack, G. (2004). Late Oligocene bunch grassland and early Miocene sod grassland paleosols from central Oregon, USA. *Palaeogeography, Palaeoclimatology, Palaeoecology*, *207*(3–4), 203–237. https://doi.org/10.1016/j.palaeo.2003.09.027

Retallack, G. (2007). Cenozoic Paleoclimate on Land in North America. Journal of Geology - J GEOL, 115, 271–294. https://doi.org/10.1086/512753

Risi, C., Muller, C., Vimeux, F., Blossey, P., Védeau, G., Dufaux, C., & Abramian, S. (2023). What Controls the Mesoscale Variations in Water Isotopic Composition Within Tropical Cyclones and Squall Lines? Cloud Resolving Model Simulations in Radiative-Convective Equilibrium. Journal of Advances in Modeling Earth Systems, 15(4), e2022MS003331. https://doi.org/10.1029/2022MS003331

Robinson, P. T., Walker, G. W., & McKee, E. H. (1990). Eocene(?), Oligocene, and lower Miocene Rocks of the Blue Mountains Region. In G. W. Walker (Ed.), Geology of the Blue Mountains Region of Oregon, Idaho, and Washington: Cenozoic Geology of the Blue Mountains Region (pp. 29–62). United States Geological Survey.

Rohrmann, A., Strecker, M. R., Bookhagen, B., Mulch, A., Sachse, D., Pingel, H., Alonso, R. N., Schildgen, T. F., & Montero, C. (2014). Can stable isotopes ride out the storms? The role of convection for water isotopes in models, records, and paleoaltimetry studies in the central Andes. Earth and Planetary Science Letters, 407, 187–195. https://doi.org/10.1016/j.epsl.2014.09.021

Ross, C. S., & Smith, R. L. (1955). Water and other volatiles in volcanic glasses*. *American Mineralogist*, *40*(11–12), 1071–1089.

Rozanski, K., Araguás-Araguás, L., & Gonfiantini, R. (1993). Isotopic patterns in modern global precipitation. Climate change in continental isotopic records, 78, 1-36.

Saylor, J. E., & Horton, B. K. (2014). Nonuniform surface uplift of the Andean plateau revealed by deuterium isotopes in Miocene volcanic glass from southern Peru. *Earth and Planetary Science Letters*, *387*, 120–131. https://doi.org/10.1016/j.epsl.2013.11.015

Seligman, A. N., Bindeman, I. N., Watkins, J. M., & Ross, A. M. (2016). Water in volcanic glass: From volcanic degassing to secondary hydration. *Geochimica et Cosmochimica Acta*, *191*, 216–238. https://doi.org/10.1016/j.gca.2016.07.010

Seligman, A. N., Bindeman, I., Van Eaton, A., & Hoblitt, R. (2018). Isotopic insights into the degassing and secondary hydration of volcanic glass from the 1980 eruptions of Mount St. Helens. Bulletin of Volcanology, 80(4), 37. https://doi.org/10.1007/s00445-018-1212-6

Smith, R. L., and R. A. Bailey. 1968. Resurgent cauldrons. Pages 613–662 in R. R. Coats, R. L. Hay, and C. A. Anderson, editors. Studies in volcanology: a memoir in honor of Howel Williams. Memoir 116. Geological Society of America, Boulder, Colorado.

Streck, M. J. (1994). Volcanology and Petrology of the Rattlesnake Ash-Flow Tuff [Oregon State University].

https://scholar.google.com/scholar_url?url=https://ir.library.oregonstate.edu/dspace/bitstream/1957/8357/1/Streck_Martin_J.pdf&hl=en&sa=X&ei=uv0AZLXpHY7gygSPuIegDA&scisig=AAGBfm3H7vSRTN-0S2T0R-fn9ynkadNnPA&oi=scholarr

Streck, M.J., and Grunder, A.L., 1995, Crystallization and welding variations in a widespread ignimbrite sheet; the Rattlesnake Tuff, eastern Oregon, USA: Bulletin of Volcanology, v. 57, p. 151–169, doi:10.1007/BF00265035.

Streck, M., & Grunder, A. (1997). Compositional Gradients and Gaps in High-silica Rhyolites of the Rattlesnake TuV. *J. Petrol., 38.* https://doi.org/10.1093/petroj/38.1.133

Streck, M. J., & Ferns, M. (2004). The Rattlesnake Tuff and Other Miocene Silicic Volcanism in Eastern Oregon (Open-File Report, pp. 5–19) [Open-File Report].

Streck, M., Ferns, M., Ricker, C., & Handrich, T. (2011). The Dinner Creek Tuff: A Widespread Co-CRBG Ignimbrite Sheet in Eastern Oregon. AGU Fall Meeting Abstracts, 2611.

Streck, M.J., and Grunder, A.L., 2012, Temporal and crustal effects on differentiation of tholeiite to calcalkaline and ferro-trachytic suites, High Lava Plains, Oregon, USA: Geochemistry, Geophysics, Geosystems, v. 13, doi:10.1029/2012GC004237.

Sundell, K. E., Saylor, J. E., Lapen, T. J., & Horton, B. K. (2019). Implications of variable late Cenozoic surface uplift across the Peruvian central Andes. Scientific Reports, 9(1), 4877. https://doi.org/10.1038/s41598-019-41257-3

Swenton, V., & Streck, M. (2022). Pre-Eruptive Magma Configurations and Petrogenetic Relationships of the Rattlesnake Tuff, Oregon–Insights From Spectacularly Banded High-Silica Rhyolite Pumices. Frontiers in Earth Science, 10. https://doi.org/10.3389/feart.2022.841279

Takeuchi, A., & Larson, P. B. (2005). Oxygen isotope evidence for the late Cenozoic development of an orographic rain shadow in eastern Washington, USA. *Geology*, *33*(4), 313. https://doi.org/10.1130/G21335.1

Tian, L., Yao, T., MacClune, K., White, J. W. C., Schilla, A., Vaughn, B., Vachon, R., & Ichiyanagi, K. (2007). Stable isotopic variations in west China: A consideration of moisture sources. Journal of Geophysical Research: Atmospheres, 112(D10). https://doi.org/10.1029/2006JD007718

USGS Water Data for the Nation. (n.d.). Retrieved March 29, 2023, from https://nwis.waterdata.usgs.gov/nwis/

Walker, G. W. (1970, June). Cenozoic Ash Flow Tuffs of Oregon. The Ore Bin, 32(6), 1–24

Waterisotopes Database. Retrieved January 12, 2022, from http://waterisotopesDB.org. Query: Country=US, Type=River or Stream, Precipitation.

Wells, Ray E. & Snavely, Parke D. (1991). *Cenozoic Evolution of the Continental Margin of Oregon and Washington* (Open-File Report) [Open-File Report]. USGS.

Zachos, J. C., & Lohmann, K. (1994). Evolution of Early Cenozoic marine temperatures. Paleoceanography, 9, 353–387. https://doi.org/10.1029/93PA03266

Zachos, J., Pagani, M., Sloan, L., Thomas, E., & Billups, K. (2001). Trends, Rhythms, and Aberrations in Global Climate 65 Ma to Present. Science, 292(5517), 686–693. https://doi.org/10.1126/science.1059412

Appendices

A – Sample and Outcrop Descriptions

Sample	dD	dD water	Lat	Long	Description	wt. % H2O
MT-13c	-169	-139	42.98389	-118.8731	Outcrop shows a variety of variously weathered tuffs, many show flow banding, fine-grained matrix with small-medium volcaniclastic clasts, pumice common. Overlain by carbonates, friable, react w/HCl. Overall, outcrop is ~20-25 ft high. Sample MT-13c is an incipiently to non-welded, white, glassy tuff with very few clasts, pumice or otherwise. Sample MT-13c was sampled from the side of RT 205 north of French Glen. Specifically, on the east side of the road, sample MT-13c was sampled from discontinuous, white glassy slightly welded bed that lies conformably below RST on the west side of the roadcut. This outcrop is visible on Google Streetview. Outcrop is not laterally extensive, appears unconformable, medium-sized clasts suggest fluvial environment? This sample location was selected by me. It is directly on the side of route 205 north of French Glen	5.1
MT-14b	-166	-136	43.02579	-118.63633	Clast-rich, moderately welded, gray-brown tuff, overlying buff moderately-welded, friable, crystal-poor tuff w/ashy matrix. Confusion about muds underlying tuff - are they conformable? sample taken from lighter, more friable basal section (MT-14a). Also sampled ash in top-most soil (MT-14b). Very fine grained, friable, ashy sandstone, some small black clasts, angular. **This is likely an older than Devine Canyon nonwelded tuff**	2.9
MT-19	-140	-110	42.84035	-119.66862	Tan-gray glassy matrix with isolated black shards. Pumices are cm-scale and show small amounts of compression by incipient welding. Field notes are not totally conclusive regarding exact sample location. Provided coordinates reflect an outcrop from lower on the hillslope that was described but not sampled. Images from the outcrop suggest this sample was collected from beneath the highest tuff cliff on the hillslope, though this can't be totally confirmed. I recommend resampling to verify sample origin.	3.4
MT-20	-151	-121	42.85964	-119.74695	Just off of Nasty Flat Rd. Extremely dense, presumably very welded tuff makes up base of ~8m outcrop. Above, slope lessens and there is abundant float of less welded, extremely glassy vitreous tuff. Red-brown, moderately welded tuff with large black rip-up tuff clast entrained in it. red-brown matrix features black and white fiamme, some isolated black shards. Sample collected from float on ridge top. Coordinates reflect exact sample location.	2.9
MT-21	-137	-107	42.78679	-120.2242	Prominent SW-facing hillslope w/various tuffs cropping out moving upward. Valley is very sandy, likely b/c of erosion tuffs above. At ridgetop, prominent outcrop is buff-red, moderately sorted, poorly welded, glassy tuff (MT-21). Gray-red, incipiently welded tuff with few red-brown lithics	3.1

					in matrix. Pumices are small (cm-scale), white, and are compressed moderately to form lens-shaped clasts (fiamme). Outcrops exhibit "flaggy" breakages and break into sheets 10-20cm thick. Sample was broken from outcrop at ridge top. Coordinates reflect precise sampling location.	
MT-23	-149	-119	43.91345	-120.30725	Gray, moderately welded tuff. glassy matrix with gray, black, and white fiamme. sample was collected from float directly beneath ridge-capping cliff-forming outcrop above. Steep talus slope made getting to the outcrop difficult. Coordinates reflect exact site of sample collection.	2.9
MT-24b	-175	-145	43.78292	-119.45026	Gray-brown, moderately welded tuff with black and white fiamme. Sample MT-24b was collected~50ft directly north of "spherulite" RST outcrop located at reported coordinates. MT-24b was found on a shallow hillslope, inferred to underlie spherulite outcrop previously described. MT-24b was broken from a larger boulder of RST, difficult to say if it is in place or float.	3
MT-25	-147	-117	43.75254	-119.00905	At top of ridge along steep-sided canyon, west side of 395. North of Burns, abundant float at top of ridge - as good as in place. Gray-brown, moderately welded tuff with black and white compressed pumices (fiamme). Matrix consists largely of clear glass shards, with some small lithics and black shards. coordinates reflect exact sample location.	2.8
MT-28b	-182	-152	43.65929	-118.99916	Sampled from the RST type section north of Burns. MT-28a corresponds with the "partially welded, vitric" lithology from Streck and Ferns (2004)	3.2
MT-28bm	-182	-152	43.65929	-118.99916	Same as MT-28b, without magnetic shards removed	2.8
MT-28a	-178	-148	43.65929	-118.99916	Sampled from the RST type section north of Burns. MT-28a corresponds with the "precursor ash deposit-clear glass shards" lithology from Streck and Ferns (2004)	2.7
MT-28d	-181	-151	43.65929	-118.99916	Sampled from the RST type section north of Burns. Mt-28d corresponds with the "nonwelded-clear and brown glass shards" layer from Streck and Ferns (2004).	2.7
MT-28dm	-181	-151	43.65929	-118.99916	Same at MT-28d without magnetic shards removed	2.7
RST2018_08	-173	-143	43.70961	-119.6356	Collected by Tessa Carlson and John Bershaw in 2018. Location referenced in Streck et al. (1999). Base is thin (what's exposed), red tuffaceous medium-grained sandstone underlying non-welded pebble-sized lapilli ash (0.5m thick)	2.9
RST2018_11	-156	-126	43.09215	-119.93541	Collected by Tessa Carlson and John Bershaw in 2018. Very thick Rattlesnake outcrop in footwall of Abert Rim, ~20miles south of Wagontire. Corresponds with Stop 8 in Streck et al. (1999). From base (basalt) 1.5m of vitric, unwelded tuff. Poorly sorted, matrix supported with pebble size pumices and lithics. Interpreted as debris flow. Top 10cm is black vitrophyre. Bottom is gradational, top is sharp. Base of white tuff intercalated with basalt below. Above is very thick (10s of meters) rheomorphic tuff that's highly deformed, largely de-vitrified, partially welded. Pebble to cobble size	2.7

					pumices. For this sample, took lowest (base of white tuff), dug ~5cm into the outcrop.	
RST2018_18	-158	-128	44.40818	-118.98748	Collected by Tessa Carlson and John Bershaw in 2018. Sampling ash at LOC 01. White ash layer sampled twice at 70cm above the base and 1.5m above the base. 60cm from the 2nd sample to contact with a partially welded, brown ash with conspicuous horizontal fractures. This brown unit was also sampled. This sample (RST_2018_18) was taken 70cm from the bottom.	3.9
M2-CVG038	-146	-116	44.52121	-119.63343	Collected by Tessa Carlson and John Bershaw in 2018. Stable isotope analyses completed by Carlson	

B – Modern δD Data

B-1 Raw Data

Latitude	Longitude	Sample ID	Type	d2H	WI Analysis Source	Project ID
45.2247	-118.513	1-15-OR18-27JUN06	Precipitation	-34.5	UAA	388
45.2247	-118.513	1-23-OR18-17JAN06	Precipitation	-150.5	UAA	388
45.2247	-118.513	1-47-OR18-24JAN06	Precipitation	-162	UAA	388
45.2247	-118.513	1-7-OR18-5JUL06	Precipitation	-58	UAA	388
44.55457	-119.642	17-040_7263	River_or_stream	-106.635	SPATIAL	98
44.24753	-120.86	BrooksStreams_704680	River_or_stream	-108.816	EPA_Corvallis	140
44.03468	-116.917	BrooksStreams_709780	River_or_stream	-118.552	EPA_Corvallis	140
45.8587	-117.636	BrooksStreams_711660	River_or_stream	-109.395	EPA_Corvallis	140
44.85146	-118.143	BrooksStreams_711680	River_or_stream	-115.189	EPA_Corvallis	140
45.19313	-118.704	BrooksStreams_714060	River_or_stream	-112.565	EPA_Corvallis	140
45.2628	-118.4	BrooksStreams_714100	River_or_stream	-105.238	EPA_Corvallis	140
44.14125	-119.291	BrooksStreams_714140	River_or_stream	-116.25	EPA_Corvallis	140
44.90149	-118.477	BrooksStreams_714160	River_or_stream	-114.804	EPA_Corvallis	140
43.77084	-118.049	BrooksStreams_717620	River_or_stream	-108.893	EPA_Corvallis	140
43.1829	-118.878	BrooksStreams_717660	River_or_stream	-109.504	EPA_Corvallis	140
45.7653	-117.76	BrooksStreams_717700	River_or_stream	-117.094	EPA_Corvallis	140
42.04489	-118.433	BrooksStreams_728640	River_or_stream	-113.95	EPA_Corvallis	140
43.86404	-116.993	BrooksStreams_730480	River_or_stream	-125.441	EPA_Corvallis	140
45.69861	-120.418	BrooksStreams_738800	River_or_stream	-125.356	EPA_Corvallis	140
44.73944	-120.328	BrooksStreams_741620	River_or_stream	-106.912	EPA_Corvallis	140
45.87203	-117.926	BrooksStreams_741840	River_or_stream	-102.031	EPA_Corvallis	140
45.73934	-119.198	BrooksStreams_741900	River_or_stream	-95.5052	EPA_Corvallis	140
45.16978	-120.482	BrooksStreams_741940	River_or_stream	-106.623	EPA_Corvallis	140
44.82284	-119.85	BrooksStreams_741960	River_or_stream	-108.44	EPA_Corvallis	140
44.63184	-119.637	BrooksStreams_741980	River_or_stream	-109.145	EPA_Corvallis	140
44.09827	-118.587	BrooksStreams_748840	River_or_stream	-116.382	EPA_Corvallis	140
45.37816	-117.653	BrooksStreams_748880	River_or_stream	-113.668	EPA_Corvallis	140
44.97614	-118.749	BrooksStreams_748980	River_or_stream	-110.704	EPA_Corvallis	140
45.63943	-117.727	BrooksStreams_749160	River_or_stream	-117.293	EPA_Corvallis	140
44.12161	-118.344	BrooksStreams_750040	River_or_stream	-116.484	EPA_Corvallis	140
42.8237	-116.808	BrooksStreams_751720	River_or_stream	-112.435	EPA_Corvallis	140
45.87269	-116.746	BrooksStreams_768020	River_or_stream	-126.525	EPA_Corvallis	140
43.78166	-116.971	CK_4338	River_or_stream	-125.5	USGS	48
43.78166	-116.971	CK_4339	River_or_stream	-125.1	USGS	48

43.78166	-116.971	CK_4340	River_or_stream	-122.6	USGS	48
43.78166	-116.971	CK_4341	River_or_stream	-122.3	USGS	48
43.78166	-116.971	CK_4342	River_or_stream	-122.2	USGS	48
43.78166	-116.971	CK_4343	River_or_stream	-122.9	USGS	48
44.24554	-116.98	CK_4344	River_or_stream	-127.4	USGS	48
44.24554	-116.98	CK_4345	River_or_stream	-128.8	USGS	48
44.24554	-116.98	CK_4346	River_or_stream	-126.1	USGS	48
44.24554	-116.98	CK_4347	River_or_stream	-125.5	USGS	48
44.24554	-116.98	CK_4348	River_or_stream	-125.2	USGS	48
44.24554	-116.98	CK_4349	River_or_stream	-124.5	USGS	48
44.24554	-116.98	CK_4350	River_or_stream	-126.8	USGS	48
44.24554	-116.98	CK_4351	River_or_stream	-126.8	USGS	48
44.24554	-116.98	CK_4352	River_or_stream	-125.1	USGS	48
44.24554	-116.98	CK_4353	River_or_stream	-123.7	USGS	48
45.61999	-117.726	CK_4371	River_or_stream	-120.2	USGS	48
45.61999	-117.726	CK_4372	River_or_stream	-116	USGS	48
45.61999	-117.726	CK_4373	River_or_stream	-118.5	USGS	48
45.61999	-117.726	CK_4374	River_or_stream	-113.4	USGS	48
45.58777	-120.408	CK_4404	River_or_stream	-110.9	USGS	48
45.58777	-120.408	CK_4405	River_or_stream	-100.8	USGS	48
45.58777	-120.408	CK_4406	River_or_stream	-108.5	USGS	48
45.58777	-120.408	CK_4407	River_or_stream	-111	USGS	48
45.58777	-120.408	CK_4408	River_or_stream	-108.3	USGS	48
45.58777	-120.408	CK_4409	River_or_stream	-96.3	USGS	48
45.62222	-120.901	CK_4410	River_or_stream	-102.8	USGS	48
45.62222	-120.901	CK_4411	River_or_stream	-103.4	USGS	48
45.62222	-120.901	CK_4412	River_or_stream	-102.4	USGS	48
45.62222	-120.901	CK_4413	River_or_stream	-105.6	USGS	48
45.62222	-120.901	CK_4414	River_or_stream	-103.3	USGS	48
45.62222	-120.901	CK_4415	River_or_stream	-103.6	USGS	48
45.62222	-120.901	CK_4416	River_or_stream	-101	USGS	48
45.62222	-120.901	CK_4417	River_or_stream	-105.6	USGS	48
45.928	-119.329	IPL-17O-IPL-18W-804	River_or_stream	-128.045	University of Michigan IsoPaleoLab	287
43.59167	-118.953	isomap_1025	Precipitation	-113.366		14
42.16167	-120.398	isomap_1041	Precipitation	-106.547		14
43.79167	-120.94	isomap_1048	Precipitation	-112.62		14
45.36812	-119.446	NRSA0809-1297	River_or_stream	-98.061	EPA	165

44.62319	-119.638	NRSA0809-1299	River_or_stream	-109.65	EPA	165
44.89843	-117.424	NRSA0809-1300	River_or_stream	-120.125	EPA	165
45.1145	-116.856	NRSA0809-1302	River_or_stream	-119.079	EPA	165
45.16978	-120.482	NRSA0809-1311	River_or_stream	-110.894	EPA	165
44.24753	-120.859	NRSA0809-1315	River_or_stream	-109.256	EPA	165
43.77084	-118.049	NRSA0809-1319	River_or_stream	-114.923	EPA	165
45.53252	-120.358	NRSA0809-1321	River_or_stream	-110.141	EPA	165
45.74943	-116.76	NRSA0809-1322	River_or_stream	-120.559	EPA	165
44.90149	-118.477	NRSA0809-1325	River_or_stream	-117.925	EPA	165
43.05277	-117.694	NRSA0809-1328	River_or_stream	-114.477	EPA	165
44.85146	-118.143	NRSA0809-1331	River_or_stream	-120.945	EPA	165
44.14125	-119.291	NRSA0809-1334	River_or_stream	-114.594	EPA	165
45.93082	-117.455	NRSA0809-1335	River_or_stream	-114.243	EPA	165
44.88502	-119.149	NRSA0809-1339	River_or_stream	-109.907	EPA	165
45.28694	-116.672	NRSA0809-1340	River_or_stream	-121.842	EPA	165
43.1829	-118.878	NRSA0809-1341	River_or_stream	-110.862	EPA	165
45.19313	-118.704	NRSA0809-1343	River_or_stream	-111.155	EPA	165
45.34631	-120.939	NRSA0809-1533	River_or_stream	-103.461	EPA	165
42.97873	-117.709	NRSA0809-1535	River_or_stream	-114.11	EPA	165
45.69861	-120.418	NRSA0809-1892	River_or_stream	-126.351	EPA	165

B-2 Modern δD Data Sources

Project ID	Contact Name	Contact Email	Citation	URL	Project Name	Proprietary
388	Phoebe Aron	paron@umich.edu	Aron, P.G., Li, S., Brooks, J.R., Welker, J.M., Levin, N.E. (2023) Seasonal variations in triple oxygen isotope ratios of precipitation in the western and central United States, Paleoceanography and Paleoclimatology	-	UM Western and Central US 17O	0
98	Lesley Chesson	lesley@isoforensics.com	personal communication, 2016	-	Isoforensics waters	0
140	J. Renee Brooks	Brooks.Reneej@epa.gov	Personal Communication	-	NRSA 2013-2014	0
48	Carol Kendall	-	Deacon, J.R., Lee, C.J., Toccalino, P.L., Warren, M.P., Baker, N.T., Crawford, C.G., Gilliom, R.G., and Woodside, M.D., 2015, Tracking water-quality of the Nationâ€™s rivers and streams, U.S. Geological Survey Web page	https://10.5066/F70G3H51	NASQAN/HBN, C. Kendall Thesis (1993)	0
287	Phoebe Aron	paron@umich.edu	Aron, P.G., Levin, N.E., Beverly, E.J., Huth, T.E., Passey, B.H., Pelletier, E.M.,	https://doi.org	UM crowdsourced	0

			Poulsen, C.J., Winkelstern, I.Z., Yarian, D.A., 2020. Triple oxygen isotopes in the water cycle. Chemical Geology 120026.	/10.1016/j.chemgeo.2020.120026	triple oxygen isotope dataset	
14	-	-	I Friedman et al (2002) Stable isotope composition of waters in the Great Basin United States. 1. Air-mass trajectories. J. Geophys. Res. 107(D19) 4400 doi:10.1029/2001JD000565	https://dx.doi.org/10.1029/2001JD000566	Great Basin Precip	0
76	Jeff Welker	jmwelker@alaska.edu	-	https://10.1002/1099-1085(20000615)14:8<1449::AID-HYP993>3.0.CO;2-7	USNIP	1
165	J. Renee Brooks	Brooks.Reneej@epa.gov	Personal Communication	https://www.epa.gov/national-aquatic-resource-surveys/nrsa	Natl Rivers and Streams Assessment 2008-2009	0
109	Adam Csank	acsank@unr.edu	-	-	WA Storm tracks	1

C – SEM Data

C-1 Oxidized vs Unoxidized Analysis

Spectrum Label	O	Na	Al	Si	Cl	K	Ca	Ti	Mn	Fe	Ni	Ba	Total
Spectrum 1	43.36	2.65	5.85	33.85	0.09	3.63	0.16			0.96			90.54
Spectrum 2	46.47	2.95	6.34	36.28		3.91	0.16			0.63			96.75
Spectrum 3	44.36	2.82	6.09	34.51		3.73	0.14			0.53			92.18
Spectrum 4	42.81	2.7	5.86	33.33	0.1	3.67	0.1			0.61			89.17
Spectrum 5	42.04	2.76	5.72	32.75	0.07	3.56	0.16	0.06		0.53			87.66
Spectrum 6	43.15	2.79	5.84	33.29	0.08	3.65	0.17			0.58			89.54
Spectrum 8	43	2.58	5.87	33.71		3.93	0.13	0.13		0.55			89.91
Spectrum 10	47.02	2.9	6.37	36.4	0.12	3.95	0.15			0.62			97.51
Spectrum 11	46.86	2.94	6.4	36.18		3.93	0.18			1.37			97.87
Spectrum 12	45.95	2.85	6.18	35.54		3.96	0.16			0.58			95.22
Spectrum 13	45.1	2.78	6.04	35.08		3.75	0.19			0.95			93.9
Spectrum 14	44.53	2.79	6.02	34.48	0.11	3.77	0.11	0.1		0.59			92.53
Spectrum 15	39.61	2.91	5.53	31.68	0.78	3.92	0.24	0.08	0.06	1.23			86.03
Spectrum 16	41.25	2.54	5.58	32.07	0.07	3.46	0.2	0.1	0.08	1.15	0.1		86.6
Spectrum 17	45.38	1.98	6.17	35.13	0.08	3.49	0.12			0.66			93.01
Spectrum 18	44.45	2.77	6.08	34.64		3.74	0.15			0.59			92.42
Spectrum 19	44.63	2.83	6.14	34.79		3.76	0.13			0.59			92.87
Spectrum 20	44.37	2.77	6.01	34.55		3.69	0.15			0.62			92.16
Spectrum 21	46.22	2.94	6.33	35.8	0.15	3.88	0.15			0.65			96.12
Spectrum 22	41.17	2.62	5.76	32.83	0.07	3.58	0.15	0.05		0.43			86.65
Spectrum 24	41.9	2.68	5.75	33.04	0.11	3.58	0.18			0.6			87.83
Spectrum 25	41	2.55	5.63	32.42	0.11	3.53	0.12			0.58			85.93
Spectrum 26	39.2	2.4	5.46	31.27	0.06	3.59	0.1	0.09		0.48			82.67
Spectrum 27	25.03	0.07	1.44	0.14	0.05	0.05	0.06	10.41	1.47	50.96			90.62
Spectrum 28	43.28	2.66	5.93	34.43		3.83	0.2			0.88			91.2
Spectrum 29	41.31	2.54	5.57	32.67		3.58	0.21			0.83			86.71
Spectrum 30	37.94	2.45	5.5	31.82	0.1	3.47	0.31			0.74			82.45
Spectrum 32	46.07	2.9	6.3	35.71	0.12	3.91	0.12			0.64			95.79
Spectrum 33	45.16	2.89	6.29	34.5		3.96	0.3			1.43			94.53
Spectrum 34	46.35	2.87	6.22	35.91		3.87	0.13	0.12		0.65			96.13
Spectrum 35	46.08	2.88	6.23	35.57		3.85	0.19			1.13			95.95

Spectrum 36	43.03	2.77	6.06	33.15		3.7	0.19	0.11		1.41			90.42
Spectrum 37	43.03	4.34	6.18	33.96		1.14	0.3			1.45		0.29	90.69
Spectrum 38	43.34	2.72	6.01	33.06		3.71	0.22	0.11		1.6			90.77
Spectrum 39	44.14	2.85	6.18	33.8	0.1	3.75	0.28	0.15		1.49			92.73
Spectrum 40	44.56	2.86	6.22	33.99		3.75	0.41			1.38		0.3	93.46
Spectrum 41	44.4	3.25	6.26	34.3		3.25	0.23	0.11	0.12	1.44			93.36
Spectrum 42	44.79	4.2	6.39	35.07		1.62	0.3	0.08		1.34			93.81
Spectrum 43	44.37	2.81	6.14	33.86		3.81	0.34	0.09		1.52			92.94
Spectrum 44	46.81	2.55	6.18	36.28	0.06	4.2	0.2	0.1	0.07	1.03			97.48
Spectrum 45	50.24	0	0	48.73		0.03	0			0			99
Spectrum 46	46.13	2.65	6.07	35.78		4.01	0.25			0.98			95.86
Spectrum 47	49.09	0	0	48.03		0	0			0.06			97.18
Spectrum 48	46.25	2.26	6.17	36.06		4.45	0.16			1.09			96.44
Spectrum 50	45.82	0	0	45.11		0.03	0			0			90.96
Spectrum 51	41.05	4.36	9.66	29.96		5.67	0.19			0.24		0.51	91.65
Spectrum 52	33.11	1.96	5.45	29.81	0.44	3.39	0.58	0.08		1.67			77.52
Spectrum 53	42.56	2.63	5.96	32.43		3.63	0.21			1.22			88.64
Spectrum 54	42.31	2.61	5.72	32.76	0.13	3.56	0.09	0.05	0.12	0.6			87.95
Spectrum 55	42.01	4.57	9.84	30.45		5.52	0.21			0.23		0.55	93.39
Spectrum 56	46.46	0.03	0	45.86		0.04	0			0			92.39
Spectrum 57	41.84	4.41	9.79	30.42		5.8	0.22			0.23		0.53	93.23
Spectrum 58	42.37	4.52	9.93	30.45		5.55	0.19			0.24		0.49	93.75
Spectrum 59	43.34	3.68	7.35	32.24		3.04	0.31			1		0.3	91.26
Spectrum 60	42.9	2.66	5.87	33.2	0.11	3.74	0.12			0.51			89.12
Spectrum 61	42.14	2.43	5.94	32.48	0.04	3.99	0.27	0.08	0.08	1.16			88.61
Spectrum 62	42.78	4.79	6.33	34.79		0.66	0.04			0.73			90.13
Spectrum 63	43.29	2.28	5.93	33.89		4.37	0.09			0.41			90.26
Spectrum 64	46.7	2.63	6.31	36.01		4.22	0.22			0.96			97.03
Spectrum 65	47.52	2.92	6.41	36.5		3.94	0.13			0.68			98.1
Spectrum 66	42.08	2.6	5.73	32.39	0.08	3.62	0.15	0.05		0.47			87.15
Spectrum 67	41.76	2.31	5.82	32.04		4.08	0.37			1.03			87.41

Spectrum 68	43.56	2.63	5.89	33.9	0.1	3.78	0.1			0.58			90.55
Spectrum 69	43.46	1.86	5.87	34.01		4.83	0.11			0.29			90.43

C-2 Treated Shard Composition

Spectrum Label	O	Na	Mg	Al	Si	K	Ca	Ti	Mn	Fe	Total
Spectrum 1	15.9	1.18	0	4.12	25.18	3.36	0.17	0.09		0.56	50.56
Spectrum 2	15.62	1.18	0.03	4.04	24.64	3.38	0.17	0.06		0.57	49.71
Spectrum 3	13.14	1.01	0	3.66	22.69	3.25	0.17	0.03		0.9	44.85
Spectrum 4	15.08	1.05	0	4.07	24.86	3.8	0.14	0.07		0.96	50.02
Spectrum 5	16.1	1.15	0	4.02	25.35	3.36	0.2	0.05		1.06	51.31
Spectrum 6	10.95	0.81	0	3.1	19.54	2.88	0.14	0.03		0.76	38.21
Spectrum 7	13.07	0.94	0.02	3.69	22.41	3.3	0.16	0.05	0.09	0.56	44.28
Spectrum 8	12.88	0.92	0	3.4	21.32	3.11	0.15	0.1	0.07	1.02	42.97
Spectrum 9	10.02	0.76	0	2.95	18.77	2.87	0.11	0	0.07	0.89	36.43
Spectrum 10	13.46	0.9	0.01	3.68	22.38	3.42	0.17	0.06	0.13	0.55	44.75
Spectrum 11	14.92	1.1	0	4.07	24.42	3.34	0.16	0.08		0.63	48.72
Spectrum 12	15.52	1.18	0	4.16	23.97	3.41	0.34	0.13		1.59	50.28
Spectrum 13	13.31	0.95	0	3.55	21.98	3.21	0.16	0.04	0.08	0.94	44.23
Spectrum 14	28.89	1.33	0	5.58	31.79	4.56	0.23	0.08		1.08	73.54
Spectrum 15	13.78	0.94	0	3.88	23.75	3.49	0.18	0.05	0.13	0.58	46.77
Spectrum 16	13.7	0.74	0	3.75	22.68	3.87	0.16	0.07		0.72	45.7
Spectrum 17	22.69	1.61	0.02	4.89	28.91	3.55	0.17	0.04		0.53	62.42
Spectrum 18	5.81	0.17	0.33	0.49	2.21	0.3	0	25.29	0.34	28.47	63.87
Spectrum 19	14.1	0.93	0	3.77	22.76	3.51	0.2	0.09		1.16	46.51
Spectrum 20	14.45	1.09	0	3.96	23.99	3.33	0.23	0.15		1.36	48.55
Spectrum 21	18.91	1	0	4.76	29.66	4.99	0.19			0.98	60.5
Spectrum 22	11.55	0.86	0	3.3	20.56	3.03	0.23	0.13		1.25	40.91
Spectrum 23	11.96	0.81	0	3.33	21.24	3.22	0.12	0.08		0.96	41.71
Spectrum 24	16.1	1.1	0	4.14	24.81	3.5	0.15	0.07		0.66	50.54
Spectrum 25	15.58	1.08	0	4.22	23.95	3.39	0.18	0.08	0.05	0.76	49.29
Spectrum 26	12.88	0.92	0	3.67	21.93	3.36	0.22	0.13	0.07	1.24	44.43
Spectrum 27	17.63	1.24	0.02	4.55	27.77	3.98	0.18	0.11		0.64	56.13
Spectrum 28	16.42	1.13	0	4.25	26.3	3.77	0.16	0.1	0.07	0.75	52.95
Spectrum 29	14.6	1	0.02	3.82	23.74	3.67	0.25	0.1		1.3	48.5
Spectrum 30	16.01	1.14	0	4.21	25.37	3.57	0.13	0	0.1	0.65	51.17
Spectrum 31	10.51	0.56	0.05	3.25	18.28	3.53	0.51	0.21		1.49	38.4
Spectrum 32	14.14	0.71	0.03	3.59	19.88	3.66	0.45	0.14		1.46	44.06
Spectrum 33	14.64	0.65	0.02	3.57	20.53	3.83	0.52	0.21		1.57	45.54
Spectrum 34	10.7	0.04	0.06	1.05	24.53	0.09	0.18	0.04		0.18	36.87
Spectrum 35	12.51	0.63	0.02	3.6	19.95	3.94	0.5	0.23		1.52	42.89
Spectrum 36	15.24	0.74	0.02	3.85	22.23	4.12	0.48	0.21		1.56	48.44
Spectrum 37	14.28	0.69	0.03	3.92	21.56	4.01	0.53	0.21		1.54	46.77
Spectrum 38	15.94	0.77	0.04	3.75	21.41	3.85	0.46	0.21		1.42	47.85
Spectrum 39	16.84	0.74	0.03	3.97	22.65	4.39	0.59	0.26		1.64	51.12
Spectrum 40	10.76	0.12	0.03	1.07	22.79	0.97	0.19	0.06		0.43	36.42
Spectrum 41	10.18	0.42	0.01	2.36	13.95	2.91	0.38	0.13		1.56	31.89
Spectrum 42	2.56	0.13	0.01	1.63	11.42	3.6	0.42	0.2		1.61	21.57
Spectrum 43	13.96	0.66	0.03	3.43	19.46	3.73	0.44	0.25		1.49	43.43
Spectrum 44	17.08	0.72	0.04	4.02	23.48	4.38	0.57	0.24		1.57	52.09
Spectrum 45	13.46	0.52	0.04	5.78	21.04	3.53	0.5	0.16		1.31	46.35
Spectrum 46	9.79	0.45	0.02	2.73	16.52	3.42	0.43	0.2		1.44	35
Spectrum 47	4.89	0.19	0.01	1.45	9.63	3.15	0.39	0.17		1.52	21.41
Spectrum 48	3.59	0.19	0.01	1.97	13.3	3.49	0.42	0.18	0.06	1.42	24.65
Spectrum 50	5.03	0.25	0.02	1.98	12.13	3.29	0.45	0.19		1.52	24.85
Spectrum 51	11.66	0.56	0.03	3.47	17.93	3.63	0.45	0.18		1.55	39.45
Spectrum 52	16.01	0.72	0.03	4.1	23.84	4.26	0.54	0.21		1.41	51.12

Spectrum 53	5.73	0.28	0.02	2.54	14.72	3.65	0.43	0.23		1.52	29.13
Spectrum 54	0.91	0.02	0	0.25	1.71	1.25	0.17	0.11		1.22	5.64
Spectrum 55	9.1	0.28	0	2.51	13.03	2.16	0.3	0.11		0.91	28.41
Spectrum 57	9.08	0.02	0	0.74	20.96	0	0.11	0.07		0.29	31.44
Spectrum 58	10.39	0.51	0.02	3.62	19.07	3.78	0.49	0.23		1.53	39.64
Spectrum 59	18.56	0.91	0.02	4.37	24.88	4.27	0.48	0.16		1.5	55.15
Spectrum 60	13.85	0.69	0.02	4.84	22.86	4.19	0.56	0.21		1.41	48.62
Spectrum 61	16	0.77	0.03	3.92	21.28	3.78	0.5	0.16		1.52	47.96
Spectrum 66	15.84	0.97	0	4.2	26.15	4.61	0.16	0.09		0.9	52.92
Spectrum 67	17.83	1	0	4.31	25.96	4.66	0.2	0	0.07	0.86	54.88
Spectrum 68	15.73	0.81	0	4	24.9	4.81	0.17	0.06	0.09	0.95	51.52
Spectrum 70	16.26	1.01	0.02	4.21	25.97	4.24	0.16	0.09	0.09	0.8	52.85
Spectrum 71	14.03	0.81	0	3.78	23.98	4.27	0.15	0.07	0.07	1.1	48.25
Spectrum 72	10.58	0.59	0.01	3.17	20.22	4.02	0.13	0.09	0.13	0.9	39.85
Spectrum 73	17.23	1.09	0	4.13	25.94	4.12	0.2	0.1	0.14	0.93	53.88
Spectrum 74	16.32	1.03	0	3.79	23.09	3.83	0.14	0.11	0.12	0.62	49.06
Spectrum 75	13.6	0.68	0	3.52	22.61	4.62	0.18	0.07	0.06	1.03	46.38
Spectrum 76	16.02	0.83	0.02	4.19	25.76	5	0.18	0.09	0.05	1.12	53.27
Spectrum 77	16.12	0.91	0	4.06	25.12	4.49	0.17	0.07	0.09	0.92	51.95
Spectrum 78	16.51	1.06	0	4.1	25.27	3.86	0.14	0.06	0.05	0.99	52.04
Spectrum 79	14.56	0.86	0	3.72	23.63	3.94	0.19	0	0.12	1.03	48.04
Spectrum 80	14.88	0.77	0	3.92	24.2	4.79	0.12	0.03	0.09	0.74	49.54
Spectrum 81	10.08	0.55	0.02	2.99	19.28	4.05	0.16	0.04	0.07	0.78	38.05
Spectrum 82	14.72	0.69	0	3.97	24.75	5.11	0.15	0.06	0	0.87	50.32
Spectrum 84	16.62	0.97	0	4.26	26.74	4.52	0.13	0.04		1.07	54.36
Spectrum 85	14.75	0.84	0.02	3.83	23.88	4.43	0.16	0	0.08	0.95	48.94
Spectrum 86	19.89	1.36	0	4.83	29.02	4.28	0.17	0.13	0.09	0.63	60.39
Spectrum 87	15.62	0.82	0	4.26	25.7	4.83	0.19	0.12	0.06	0.96	52.56
Spectrum 88	15.96	0.99	0	3.91	24.42	4.04	0.14			0.93	50.39
Spectrum 89	7.61	0.46	0	1.87	12.53	2.92	0.11	0.03	0.06	0.56	26.15
Spectrum 90	10.32	0.55	0.01	3.18	20.62	4.3	0.16	0.06	0.04	0.99	40.22
Spectrum 91	18.78	0.82	0	4.45	26.85	5.17	0.15	0.12		1.05	57.4
Spectrum 92	18.47	1.05	0	4.62	27.91	5.06	0.18	0.1	0.11	0.6	58.09
Spectrum 93	17.54	0.9	0	4.26	26.62	5.08	0.15	0.09		0.96	55.61
Spectrum 96	8.84	0.55	0	2.55	16.64	3.27	0.13			0.84	32.83
Spectrum 97	11.23	0.59	0	2.95	18.9	4.17	0.14	0.04	0.04	0.74	38.8
Spectrum 98	14.65	0.83	0	3.82	23.88	4.54	0.16			0.74	48.62
Spectrum 99	11.28	0	4.4	0.04	0.15	0.08	23.54			0	45.06
Spectrum 100	14.11	0.76	0	3.86	24.19	4.83	0.13	0.09	0.08	0.89	48.95
Spectrum 101	14.28	1.08	0	3.68	23.75	3.55	0.16	0.1	0.07	0.84	47.51
Spectrum 102	5.48	0.37	0	1.85	12.53	2.7	0.1	0.04	0.04	0.54	23.65
Spectrum 104	0.53	0	0	0.17	59.32	0	0			0.08	60.11
Spectrum 105	0.69	0.02	0	0.15	53.8	0.03	0	0.04		0	54.74
Spectrum 106	0.88	0	0	0.43	52.62	0	0			0	53.93
Spectrum 107	14.27	0.99	0.04	3.63	22.77	3.61	0.11			0.58	45.98
Spectrum 108	8.95	0.62	0	2.87	19.1	3.68	0.12	0.07	0.05	0.77	36.22
Spectrum 109	15.29	1.02	0	3.96	25.09	4.06	0.16	0.11	0.09	0.77	50.55
Spectrum 110	11.81	0.68	0	3.2	20.58	4.18	0.14	0.05	0.07	0.78	41.49
Spectrum 111	17.51	1.11	0.02	4.39	27.65	4.85	0.18	0.08	0.06	0.62	56.45

Spectrum 112	22.07	1.49	0	5.04	30.47	4.48	0.19	0.08	0.07	0.58	64.46
Spectrum 113	12.5	0.87	0	3.3	20.96	3.63	0.12	0.07		0.59	42.03
Spectrum 114	16.1	1.14	0	3.95	24.05	3.67	0.17			0.54	49.63
Spectrum 115	26.03	1.53	0	5.11	31.2	4.95	0.17	0.11	0.08	0.62	69.81
Spectrum 116	12.63	0.9	0	3.55	22.78	3.68	0.17	0.05	0	0.62	44.38
Spectrum 117	4.82	0.27	0	1.74	11.54	2.99	0.08	0.06	0.07	0.52	22.08
Spectrum 118	13.08	0.96	0	3.38	21.47	3.28	0.13	0.12	0.04	0.59	43.05
Spectrum 119	3.47	0.23	0.01	1.55	11.66	3.46	0.1	0.07	0	0.55	21.11
Spectrum 120	15.41	1.17	0.01	3.96	24.75	3.59	0.17	0.07	0.07	0.56	49.75
Spectrum 121	14.57	1.09	0.02	3.87	24.21	3.55	0.13	0.06	0.09	0.61	48.2
Spectrum 122	14.75	1.08	0	3.73	23.66	3.62	0.14		0.06	0.72	47.76
Spectrum 123	14.88	1.08	0	4.03	25.15	3.99	0.16	0.1	0.08	0.58	50.04
Spectrum 124	16.39	1.28	0	4.08	25.5	3.48	0.15	0.05	0.08	0.61	51.62
Spectrum 125	9.32	0.54	0	2.83	18.41	3.85	0.13	0.06	0.1	0.83	36.06
Spectrum 126	15.83	0.96	0	4.02	25.22	4.35	0.16	0.08	0.12	0.77	51.52
Spectrum 127	12.48	0.77	0	3.18	20.37	3.85	0.12	0.05		0.63	41.44
Spectrum 128	9.05	0.27	0	2.07	13.12	3.9	0.06	0.06	0.05	0.45	29.02
Spectrum 129	2.21	0.1	0	0.75	6.5	2.26	0.1	0.04	0.06	0.28	12.3
Spectrum 130	16.97	1.03	0	4.23	25.87	4.47	0.17	0.05	0.07	0.78	53.64
Spectrum 132	15.85	1.14	0.02	5.19	24.75	3.46	0.13	0.08		0.59	51.21
Spectrum 133	12.38	0.89	0	4.54	20.36	3.29	0.12	0.1		0.59	42.27
Spectrum 134	14.9	1.02	0.01	5.27	22.47	3.42	0.12	0.06		0.81	48.09
Spectrum 135	12.69	0.91	0	4.01	21.54	3.38	0.1	0.07	0	0.57	43.29
Spectrum 136	17.67	1.03	0	5.75	25.49	4.03	0.15	0.07		0.36	54.56
Spectrum 137	13.33	0.96	0	4.25	22.49	3.51	0.08	0.05		0.5	45.17
Spectrum 138	11.91	0.82	0	3.4	19.45	3.05	0.08	0.06	0	0.49	39.26
Spectrum 139	12.49	0.91	0	3.81	20.8	3.13	0.11	0.07	0	0.56	41.87
Spectrum 140	10.84	0.77	0.01	3.69	18.7	2.89	0.12	0.08	0	0.78	37.87
Spectrum 141	12.19	0.8	0.01	4.12	21.23	3.54	0.1	0.07		0.52	42.59
Spectrum 142	13.65	0.96	0	4.72	21.42	3.16	0.14	0.04		0.51	44.6
Spectrum 143	14.5	1.02	0	5.32	22.76	3.55	0.12	0.07		0.53	47.87

Spectrum 144	13.95	1.01	0	4.88	23.98	3.59	0.13	0		0.66	48.2
Spectrum 145	14.05	1.03	0	4.47	22.52	3.33	0.12	0.08		0.67	46.26
Spectrum 146	11.53	0.74	0.02	4.18	20.08	3.39	0.14	0.08		0.6	40.75
Spectrum 147	13.09	0.92	0	4.08	21.25	3.57	0.1	0		0.37	43.38
Spectrum 148	18.69	1.32	0	5.16	27.25	3.87	0.15	0.05		0.66	57.15
Spectrum 149	17.26	1.19	0	5.39	26.09	3.72	0.14	0.08		0.59	54.45
Spectrum 150	13.92	0.95	0.02	4	22.13	3.42	0.1	0.09		0.5	45.12
Spectrum 151	12.55	0.86	0	4.53	20.39	3.34	0.11	0.07		0.38	42.22
Spectrum 152	17.03	1.13	0.03	5.96	24.07	3.64	0.05	0.06	0.07	0.52	52.55
Spectrum 153	14.65	0.96	0	4.54	23.29	3.76	0.1	0.11		0.63	48.04
Spectrum 154	13.56	0.86	0.02	4.29	22.51	3.7	0.15	0.1	0.05	0.6	45.84
Spectrum 155	13.02	0.93	0	4.41	21.13	3.1	0.08	0.06		0.6	43.34
Spectrum 156	14.1	0.96	0.01	4.69	23.05	3.59	0.1	0.1	0	0.52	47.11
Spectrum 157	12.79	0.94	0	4.49	21.37	3.32	0.11	0.04		0.63	43.69
Spectrum 158	13.4	0.94	0.02	4.15	22	3.61	0.07	0.08		0.6	44.87
Spectrum 159	16.52	1.05	0	7.54	24.27	3.81	0.14	0.09		0.9	54.31
Spectrum 160	17.38	1.02	0	9.35	22.32	3.27	0.15	0.09		0.56	54.13
Spectrum 161	15.15	0.36	0	22.93	10.07	2.08	0.17	0		0.34	51.09
Spectrum 162	12.39	0.86	0	4.21	19.65	3.1	0.46	0.05		0.52	41.51
Spectrum 163	13.87	0.39	0	19.67	10.52	1.99	0.14	0.05		0.28	46.91
Spectrum 164	17.9	1.16	0.03	5.97	24.17	3.6	0.1	0.09		0.57	53.59
Spectrum 165	13.75	0.91	0	5.09	22.32	3.63	0.11	0.08		0.54	46.43
Spectrum 166	14.4	1.01	0	5.45	21.92	3.27	0.1	0.09	0.06	0.54	46.84